X. PLASMAS AND CONTROLLED NUCLEAR FUSION

A. Active Plasma Systems*

Academic and Research Staff

Prof. L. D. Smullin
Prof. A. Bers
Prof. R. J. Briggs
Prof. R. R. Parker

Graduate Students

D. S. Guttman
F. Herba
B. R. Kusse
Y-Y. Lau
R. K. Linford
J. A. Mangano
J. A. Rome
H. M. Schneider

1. INTERACTION OF A SPIRALING ELECTRON BEAM AND A PLASMA

The spiraling electron beam waves have been previously described.[1] The theory has now been extended to include the effects of a background plasma and finite transverse geometry. Several instabilities result. The wavelength and frequency of the instability with the largest growth rate appears to agree with oscillations that we have observed in our spiraling electron beam plasma experiment.

The model studied is described in Fig. X-1. The electron beam is assumed to have a square spatial distribution. It has velocity components along and across the axial magnetic field. The beam is positioned between two conducting cylinders. The region

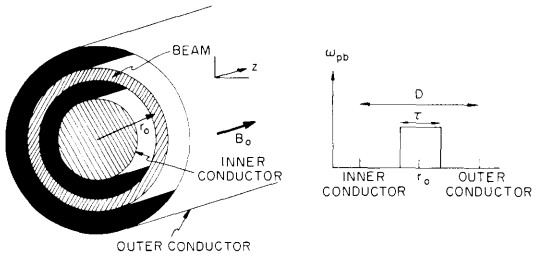

Fig. X-1. Cylindrical geometry and beam distribution.

between the cylinders is uniformly filled with a plasma of electrons and infinitely massive ions. Small-signal perturbations were assumed to be of the form $e^{j(\omega t - m\theta - kz)}$, where ω is the radian frequency, and m and k are the azimuthal and axial wave numbers. The cylindrical beam was unwrapped[1] and a rigid beam analysis performed.[2] The dispersion relation that results for interactions between the beam space-charge waves and the plasma waves can be put in the following form

*This work was supported by the National Science Foundation (Grant GK-2581).

$$(\omega - m\omega_c - kv)^2 = \frac{\omega_B^2 k^2}{k^2 K_{\parallel} + \left(\frac{m^2}{r_o^2} + p^2\right) K_{\perp}}, \tag{1}$$

where

$$K_{\perp} = 1 - \frac{\omega_p^2}{\omega^2 - \omega_c^2}; \qquad K_{\parallel} = 1 - \frac{\omega_p^2}{\omega^2}.$$

Here, ω_c is the electron cyclotron frequency, ω_p the electron plasma frequency, v the axial beam velocity, r_o the mean radius of the beam, and p the radial wave number. ω_B is a reduced beam-plasma frequency given by

$$\omega_B^2 = \frac{8\omega_{pb}^2 \sin^2 \frac{p\tau}{2}}{\tau D p^2},$$

where D is the distance between the cylinders, τ is the beam thickness, and ω_{pb} is the beam-plasma frequency. The interaction between the beam cyclotron waves and the plasma waves can be placed in the following form:

$$(\omega - m\omega_c - kv)^2 - \omega_c^2 = \frac{\omega_B^2 \frac{m^2}{r_o^2}}{k^2 K_{\parallel} + \left(p^2 + \frac{m^2}{r_o^2}\right) K_{\perp}}. \tag{2}$$

The unstable interaction regions are shown in Fig. X-2. The uncoupled beam and plasma waves have been drawn for the cases m = 1 and m = 2. Equation 1 describes the interactions numbered 1, 3, 5, and 7, while Eq. 2 holds for interactions 2, 4, 6, and 8.

The Bers-Briggs stability criteria were used and applied to each of these interactions. All except the coupling at 4 are backward-wave interactions and absolutely unstable in an infinite-length system. They all have starting lengths and a starting frequency in finite-length systems.[4] The interaction in region 4 is convectively unstable in an infinite-length system. These interactions were investigated for the plasma parameters of our experiment.

The e-folding length for the convective instability was found to be several times our system length. The starting lengths for interactions 3, 7, and 8 are also many-system lengths. The starting lengths for interactions 1, 2, 5, and 6 are all less than a system length. The growth rates for the absolute instability at interactions 1 and 5 are, however, approximately twice the growth rates at 2 and 6. The interactions at 1 and 5 also

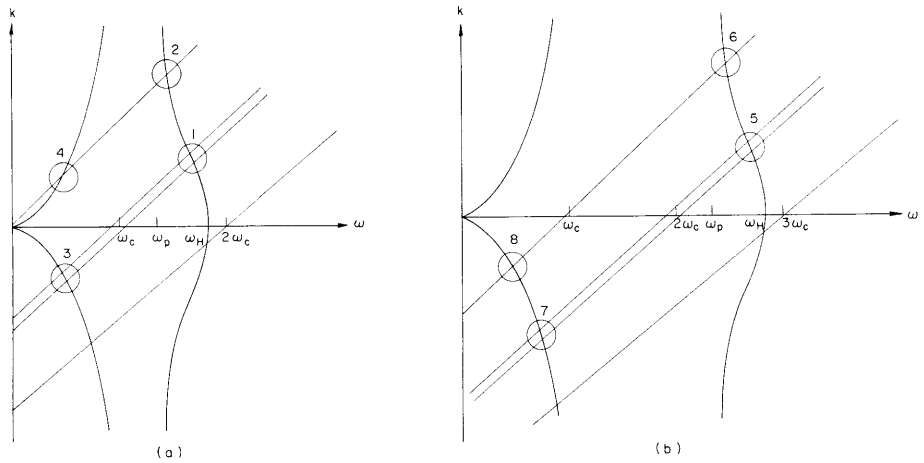

Fig. X-2. Uncoupled beam and plasma waves: (a) for m = 1; (b) for m = 2.

give frequencies and wavelengths that are in good agreement with the observed values. Two comparisons are shown in Figs. X-3 and X-4.

In Fig. X-3 the vertical position of a data point was determined by the value of the observed frequency, the horizontal position by using experimentally observed values for

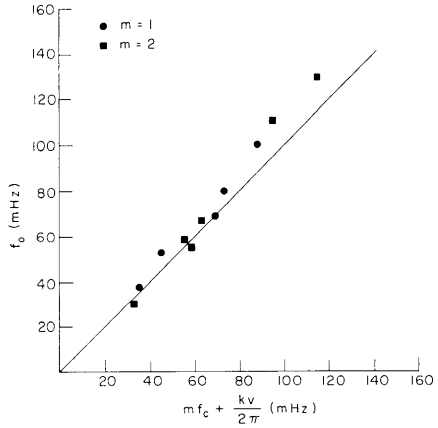

Fig. X-3. Observed frequency vs beam space-charge wave Doppler shift.

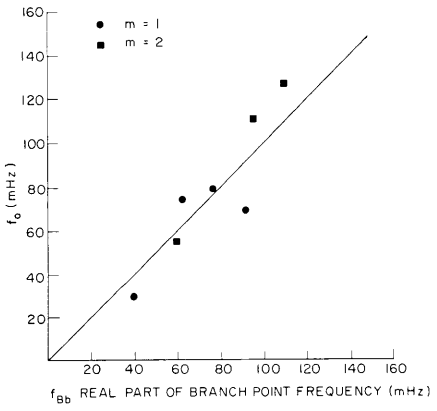

Fig. X-4. Observed frequency vs predicted frequency for infinite-length system.

wavelength, v, m, and ω_c. Similarly, the vertical position in Fig. X-4 was determined by the observed frequency, and the horizontal position by the real part of the frequency of the absolute instability given by Eq. 1 with experimental values for the plasma parameters.

The beam space-charge wave interaction with the backward plasma wave appears to describe the observed oscillations. At present, we are investigating the role of collisions, thermal effects, and the finite lengths of the systems.

B. R. Kusse

References

1. B. R. Kusse and A. Bers, "Spiraling Beam-Plasma Interactions," Quarterly Progress Report No. 88, Research Laboratory of Electronics, M.I.T., January 15, 1968, pp. 175-182.
2. A. Bers, "Theory of Beam-Plasma Interactions," Quarterly Progress Report No. 85, Research Laboratory of Electronics, M.I.T., April 15, 1967, pp. 163-167.
3. R. J. Briggs, Electron-Stream Interactions with Plasmas (The M.I.T. Press, Cambridge, Mass., 1964).
4. H. R. Johnson, "Backward-Wave Oscillators," Proc. IRE 43, 684-697 (1955).

2. NONLINEAR AND NONLAMINAR OSCILLATIONS IN INHOMOGENEOUS PLASMAS

Introduction

In a previous report,[1] the computer simulation of a cold, inhomogeneous plasma that was simulated had an equilibrium density $n_o(x) = n_c/(1+x^2)$ and the electrons were given a uniform displacement at t = 0. The voltage across the plasma was compared with the results of a linearized fluid description of the electron dynamics.

To give a more complete treatment of the details of the electron motion, the build-up of the electron density as a function of time is presented here, and it is shown that local nonlinearities occur before nonlaminar motion[2] takes place. The results of the computer simulation will be compared with the density as derived from linearized fluid theory. Furthermore, a linearized Lagrangian analysis of the electron dynamics[2] will be used to find the electron density; this approach correctly describes the density well into the nonlinear regime, and is valid until an overtaking occurs.

Finally, the state of the plasma after overtakings occur will be discussed. The spreading of the nonlaminar motion and randomization of electron velocities in a plasma with such a smooth density gradient is similar to the effects noted previously for a sharply bounded plasma.[3]

Lagrangian Formulation of Electron Density

The equation of motion for an electron in a cold inhomogeneous plasma is[2]

$$\frac{d^2x}{dt^2} = -\int_{x_o}^{x} \omega_p^2(x')\, dx', \tag{1}$$

where $x = x(x_o, t)$ is the instantaneous position of an electron whose equilibrium position is x_o, and ω_p is the local plasma frequency. The integral on the right-hand side of Eq. 1 may be expanded in a Taylor series about x_o to give for the equation of motion

$$\frac{d^2x}{dt^2} = -\left[(x-x_o)\,\omega_p^2(x_o) + \frac{1}{2}(x-x_o)^2\,\frac{d\omega_p^2(x_o)}{dx} + \ldots\right]. \tag{2}$$

Equation 2 holds as long as no overtaking has occurred.[3]

As long as the displacement from equilibrium is small, in the sense that the second term on the right side of Eq. 2 is small compared with the first, namely

$$|x-x_o| \ll \left|\frac{\omega_p(x_o)}{\omega_p'(x_o)}\right|, \tag{3}$$

the differential equation (2) will be linear in $(x-x_o)$, and has the simple solution

$$x - x_o = A \cos \omega_p(x_o)\, t + B \sin \omega_p(x_o)\, t. \tag{4}$$

It is interesting to note that the linearization condition (3) has the interpretation that the excursion of an electron must be small compared with the scale length of the gradient in ω_p.

For an initial displacement perturbation of amplitude δ, where the initial conditions are $x(x_o, t=0) = x_o + \delta$ and $\left.\frac{dx}{dt}\right|_{t=0} = 0$, the solution (4) becomes

$$x = x_o + \delta \cos \omega_p(x_o)\, t. \tag{5}$$

The density of electrons can be obtained from Gauss' law

$$n(x,t) = n_o(x) - \frac{\epsilon_o}{e}\frac{\partial E}{\partial x}, \tag{6}$$

where E is the electric field in the plasma at a fixed point. From the linearized equation of motion (2) the electric field acting on a particle at position x is

$$E(x, x_o) = \frac{m}{e}\omega_p^2(x_o)[x-x_o] \tag{7}$$

so the electron density (6) becomes

$$n = n_o(x) - \frac{\epsilon_o}{e}\frac{\partial E}{\partial x_o}\frac{\partial x_o}{\partial x} = n_o(x) - n_o(x_o) + \frac{\partial x_o}{\partial x}\left[n_o(x_o) - (x-x_o)\frac{\partial n_o(x_o)}{\partial x_o}\right]. \tag{8}$$

The density is given as a function of x, once the inversion of Eq. 5 to obtain $x_o = x_o(x, t)$ has been carried out. Note that the quantity $\partial x_o/\partial x$ appearing in (8) can be written (by using Eq. 5) as

$$\frac{\partial x_o}{\partial x} = \frac{1}{1 - \delta\,\omega_p'(x_o)\,t\,\sin\left[\omega_p(x_o)\,t\right]}, \tag{9}$$

and hence this is also a function of x, once $x_o = x_o(x, t)$ has been found. The inversion of Eq. 3 has been carried out numerically so that a comparison could be made with the computer experiments and the results are given below.

The numerical solution of (5) is not required at t = 0. In this case the solution can be obtained from (5) directly:

$$x_o(x, t=0) = x - \delta \tag{10}$$

and

$$\frac{\partial x_o}{\partial x} = 1. \tag{11}$$

The electric field (from Eq. 7) is

$$E(x, t=0) = \frac{e\delta}{\epsilon_o} n_o(x-\delta), \tag{12}$$

and the electron density (from Eq. 8) is

$$n(x, t=0) = n_o(x) - \delta n_o'(x-\delta). \tag{13}$$

The Lagrangian theory is linear only in the sense that the equation of motion is linear. The electric field and electron density are not linear functions of the displacement δ. The electron density contains terms proportional to $\partial x_o/\partial x$ which becomes infinite at the time of overtaking.[2] The theory is valid up to this point, and hence should predict the density more accurately than the linearized fluid description in which it is assumed that the perturbation density $n_1 \ll n_o$.

Build-up of Large-Amplitude Electron Densities

The electron density in a plasma with density $n_o(x) = n_c/(1+x^2)$ was simulated when the initial displacement $\delta = 0.1$. As was reported previously,[1] the first overtaking occurs at a time $t/T_{pc} = 4.16$, where T_{pc} is a plasma period of the electrons at x = 0. The total electron density as found from the simulation is shown for two times before overtaking in Figs. X-5 and X-6. The bar graphs in the figures are the results of

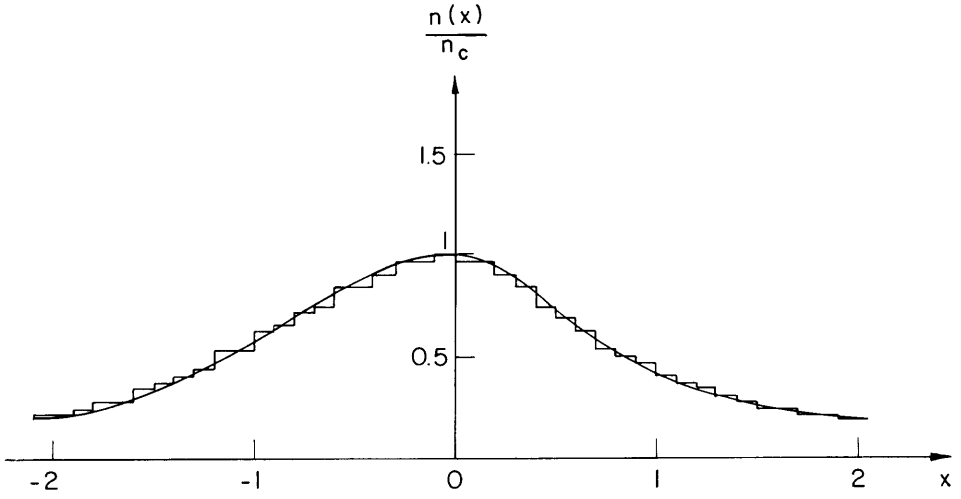

Fig. X-5. Total electron density at $t/T_{pc} = 0.56$.

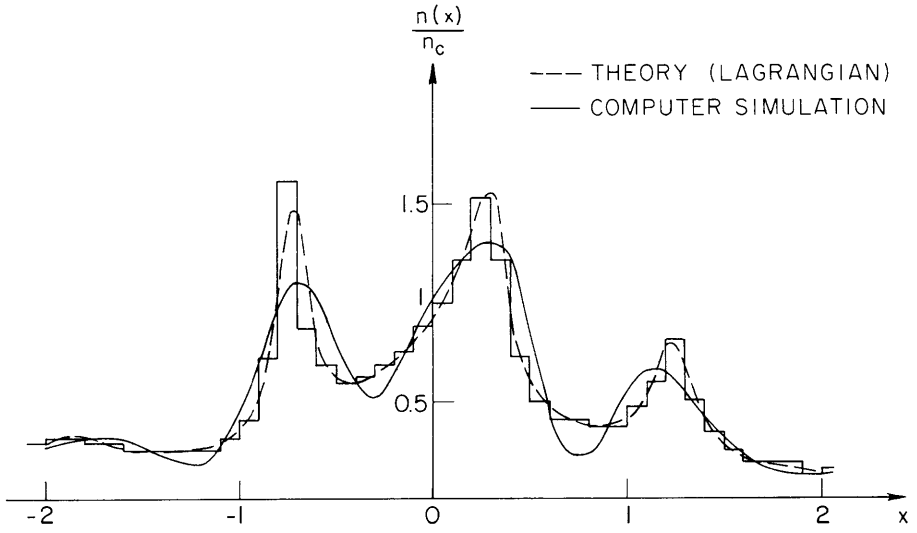

Fig. X-6. Total electron density at $t/T_{pc} = 2.82$.

counting electron sheets in "cells" having width 0.1. The dashed line in these figures is the electron density as calculated from the Lagrangian theory (Eqs. 5, 8, and 9). The solid line is the density as calculated from a linearized fluid or Eulerian theory.[4] In Fig. X-5, all three curves are in good agreement, and the dashed line coincides with the solid line. In Fig. X-6, however, the density from the simulation has local nonlinearities or "spikes," which are accurately predicted by the Lagrangian theory. The Eulerian theory is really invalid near these points, since the first-order density is not much less than the equilibrium density, and this theory does not agree with the simulation results near those points.

Nonlaminar Effects

In order to investigate the state of the plasma after the first crossing occurs, a large-amplitude perturbation of $\delta = 0.5$ was made. This was done so that crossings occurred earlier in order to cut computation costs.

The first overtaking was found to occur at $t/T_{pc} = 0.99$. The way in which the nonlinear motion spreads into the plasma is shown in Fig. X-7; the solid lines show the

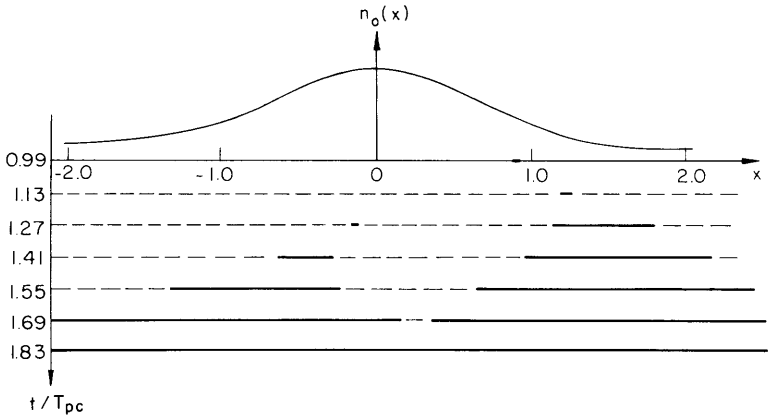

Fig. X-7. Spreading of nonlaminar motion as a function of time (solid lines indicate where overtaking has occurred).

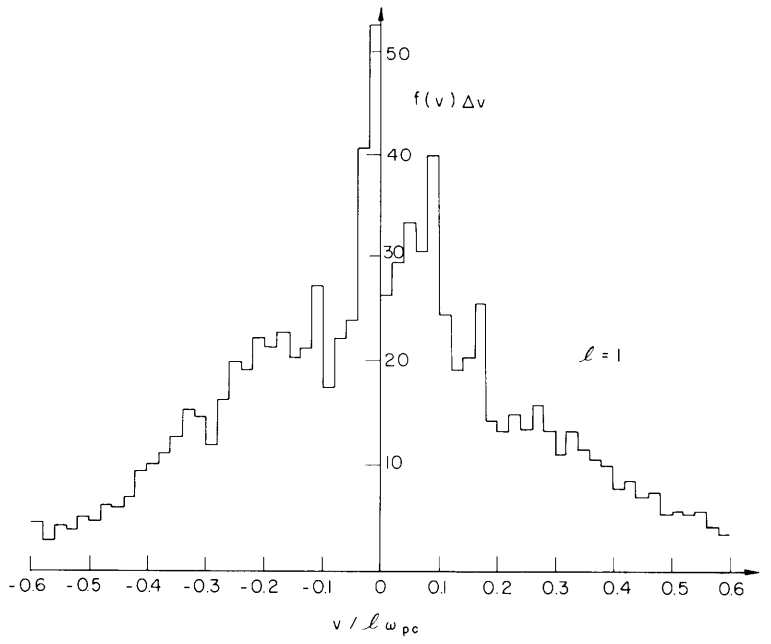

Fig. X-8. Time-average velocity distribution.

regions in the plasma at which crossings have occurred. Note that by the time $t/T_{pc} = 1.8$ the nonlinear motion has spread through the center of the plasma.

The distribution in velocities of the electron sheets at $t = 3T_{pc}$ is shown in Fig. X-8. The distribution was obtained by averaging over one period of oscillation (measured at $x = 0$) and the energy in the distribution was found. The total kinetic energy of the randomizing particles is found to be

$$U = 0.03\pi m\omega_{pc}^2 n_c,$$

while the total initial energy given to the plasma in the uniform displacement perturbation is

$$U_o = 0.06\pi m\omega_{pc}^2 n_c.$$

Hence, about one half of the original energy has gone into random motion. For much later times complete randomization should be observed.

H. M. Schneider

References

1. H. M. Schneider, Quarterly Progress Report No. 89, Research Laboratory of Electronics, M.I.T., April 15, 1968, pp. 127-130.
2. H. M. Schneider and A. Bers, "Nonlinear Effects in Plasma Slab Oscillations," Symposium on Computer Simulation of Plasma and Many Body Problems, Williamsburg, Virginia, April 1967.
3. H. M. Schneider, Quarterly Progress Report No. 84, Research Laboratory of Electronics, M.I.T., January 15, 1967, pp. 149-151.
4. A. Bers and H. M. Schneider, Quarterly Progress Report No. 89, op. cit., pp. 123-126.

3. STEADY-STATE OSCILLATIONS IN INHOMOGENEOUS PLASMAS

Introduction

Previous reports[1, 2] on oscillations in inhomogeneous plasmas have been concerned with nonlinear and nonlaminar effects that occur in the transient response of a plasma to initial density or velocity perturbations. In the steady state, nonlinear effects will also be important near the cold-plasma resonance point, unless some physical mechanism limits the nonlinearity.

In this report, the response of a cold inhomogeneous plasma to a steady-state driving field will be discussed. Three mechanisms for limiting the nonlinearity are described: collisions, a spread in oscillator frequency, and thermal effects.

The impedance of the plasma will be calculated and it will be shown how the

inhomogeneity in plasma density contributes a real part to this impedance. The relationship of the real part of the impedance to the power dissipated in collisions and thermal motion is also discussed.

Inhomogeneous Cold-Plasma Response

In a one-dimensional inhomogeneous cold plasma with density $n_o(x)$ the electric field is given by $E(-\infty, \omega)/\epsilon(x, \omega)$, where $E(-\infty, \omega)$ is the Fourier transform of the electric field at $x = -\infty$ (the point at which the plasma density is assumed to be zero), and $\epsilon(x, \omega)$ is the relative plasma dielectric constant. In the absence of collisions the field is given by

$$E(x, \omega) = \frac{E(-\infty, \omega)}{1 - \frac{\omega_p^2(x)}{\omega^2}}, \tag{1}$$

where $\omega_p(x)$ is the local electron plasma frequency. In Eq. 1, the motion of the ions has been neglected because they are assumed to form a stationary neutralizing background.

When the electric field at $x = -\infty$ is a single-frequency source such as

$$E(-\infty, t) = \cos \omega_o t \tag{2}$$

the plasma electric field becomes

$$E(x, t) = \frac{\cos \omega_o t}{1 - \frac{\omega_p^2(x)}{\omega_o^2}}. \tag{3}$$

Note that at the points in the plasma where the driving frequency ω_o is equal to the local plasma frequency, $\omega_o = \omega_p(x)$, the field in (3) exhibits a resonance. Nonlinear effects are obviously important near this point unless other physical effects become dominant near the resonance point. Three mechanisms that can limit the amplitude of the field at this point will now be described.

Collisions

In a one-dimensional plasma with collisions described by a collision frequency ν the electric field in the plasma is

$$E(x, \omega) = \frac{E(-\infty, \omega)}{1 - \frac{\omega_p^2(x)}{\omega(\omega - j\nu)}}. \tag{4}$$

Near the resonance point the denominator of (4) may be expanded for small ν/ω, and the response to a driving field $E(-\infty, t) = \cos \omega_o t$ becomes

$$E(x, t) = -\frac{\omega_p}{\nu} \sin \omega_p t \tag{5}$$

$$\frac{\nu}{\omega_p} \ll 1 \tag{6}$$

at the resonance point $\omega_o = \omega_p$. The field thus becomes infinite as ω_p/ν, for small collision frequency. If we use the fact that the first-order electron density is $n_1(x, \omega) = -(\epsilon_o/e)\, \partial E/\partial x$, the time-dependent density at the resonance point is

$$n(x, t) = -\frac{\epsilon_o}{e} \frac{\left(\omega_p^2\right)'}{\nu^2} \cos \omega_p t. \tag{7}$$

The power dissipated in this plasma has been shown by Gil'Denburg,[3] and Briggs and Paik[4] to be independent of the collision frequency ν in the limit as ν approaches zero. This can be seen by writing the power dissipated as

$$P = \frac{1}{2} \mathrm{Re} \int_{-\infty}^{\infty} \sigma |E|^2 \, dx, \tag{8}$$

where the plasma conductivity[5] is

$$\sigma = \frac{j\omega\epsilon_o\omega_p^2}{\omega^2}\left(1 + j\frac{\nu}{\omega}\right) \qquad \nu/\omega \ll 1. \tag{9}$$

Using the expression for E given by (4) in the limit of $\nu/\omega \ll 1$, the power dissipated becomes

$$P = \frac{1}{2} \frac{\epsilon_o\omega_p^2}{\omega^2} |E(-\infty, \omega)|^2 \int_{-\infty}^{\infty} \frac{\nu \, dx}{\left[1 - \frac{\omega_p^2}{\omega^2}\right]^2 + \frac{\omega_p^4}{\omega^4}\frac{\nu^2}{\omega^2}}. \tag{10}$$

As the collision frequency ν goes to zero, the major contribution to the integral in (10) comes from the vicinity of the resonance point $\omega = \omega_p(x)$. Expanding the denominator in the integral (10) gives the result

$$P = \frac{\pi}{2} \epsilon_o \frac{\omega^3}{\left(\omega_p^2\right)'} |E(-\infty, \omega)|^2 \tag{11}$$

in the limit of ν going to zero. The prime denotes differentiation with respect to x. Note that the power dissipated (Eq. 11) is independent of ν in the limit of ν going to zero.

Spread in Oscillator Frequency

If the driving electric field has a spread in frequencies about ω_o, the electric field near the cold plasma resonance point remains finite. As an example, suppose the electric field $E(-\infty, \omega)$ has the form

$$E(-\infty, \omega) = \frac{\sqrt{\pi}}{\delta\omega}\left[\exp\left\{\frac{-(\omega-\omega_o)^2}{\delta\omega^2}\right\} + \exp\left\{\frac{-(\omega+\omega_o)^2}{\delta\omega^2}\right\}\right] \tag{12}$$

which is shown as a function of ω for the case $\delta\omega \ll \omega_o$ in Fig. X-9. The time-dependent driving field which is the inverse transform of Eq. 12 is

$$E(-\infty, t) = \exp\left[-\frac{1}{4}(\delta\omega)^2 t^2\right] \cos \omega_o t, \tag{13}$$

which reduces to the steady-state drive at ω_o as $\delta\omega \to 0$. (Note that in this limit the transform $E(-\infty, \omega)$ approaches a pair of impulses having area π at $\omega = +\omega_o$ and $\omega = -\omega_o$,

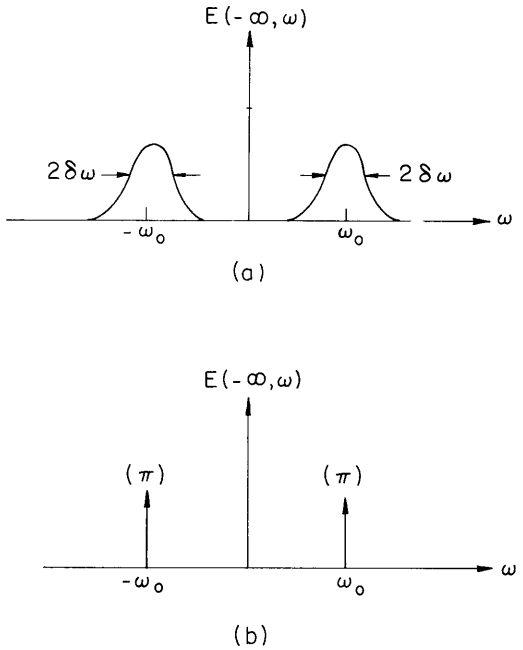

Fig. X-9. (a) Transform of the field if the source has a spread $\delta\omega$ in frequency about ω_o.
(b) Transform of the field if $\delta\omega \to 0$ (a steady-state source at ω_o).

as is also shown in Fig. X-9.)

Multiplying $E(-\infty, \omega)$ by $1/\left(1-\omega_p^2/\omega^2\right)$ to obtain the field inside the plasma and inverse transforming gives

$$E(x,t) = \exp\left[-\frac{1}{4}\delta\omega^2 t^2\right] \cdot \left[\cos\omega_o t - \frac{\omega_p}{2\delta\omega}\,\mathrm{Re}\left\{e^{j\omega_o t}\, Z\left(-\frac{\omega_o}{\delta\omega} - \frac{\omega_p}{\delta\omega} - j\,\frac{\delta\omega t}{2}\right)\right.\right.$$

$$\left.\left. + e^{-j\omega_o t}\, Z\left(\frac{\omega_o}{\delta\omega} - \frac{\omega_p}{\delta\omega} - j\,\frac{\delta\omega t}{2}\right)\right\}\right], \qquad (14)$$

where $Z(\xi)$ is the plasma dispersion function,[6]

$$Z(\xi) = \frac{1}{\sqrt{\pi}}\int_{-\infty}^{\infty}\frac{e^{-x^2}\,dx}{x-\xi} \qquad \mathrm{Im}\,\xi > 0 \qquad (15)$$

and the relation $Z(-\xi^*) = -[Z(\xi)]^*$ has been used in obtaining (14). To find the behavior of the electric field near the resonance point, let ω_o approach ω_p in (14). By using appropriate expansions[6] of Z as $\delta\omega$ becomes small, the field at the point $\omega_o = \omega_p$ may be written

$$E(x,t) = \exp\left[-\frac{1}{4}\delta\omega^2 t^2\right]\left[\cos\omega_p t - \frac{\sqrt{\pi}\,\omega_p}{2\delta\omega}\sin\omega_p t\right]. \qquad (16)$$

Thus the electric field becomes infinite at $\omega_o = \omega_p$ as $(\omega_p/\delta\omega)$ in the limit of small $\delta\omega$.

The first-order charge density near the resonance point can be found from Gauss' law again, $n_1 = -(\epsilon_o/e)\,\partial E/\partial x$, with the result that

$$n_1(x,t) = \frac{\epsilon_o}{e}\,\frac{\omega_p\omega_p'}{\delta\omega}\exp\left[-\frac{1}{4}\delta\omega^2 t^2\right]\cos\omega_p t, \qquad (17)$$

which shows that the density becomes infinite as $\left(\omega_p^2\right)'/\delta\omega^2$.

Thermal Effects

When the electrons in an inhomogeneous plasma have nonzero temperature, nonlocal effects are introduced and the singularity in the electric field at the point $\omega = \omega_p(x)$ vanishes. The problem of wave propagation in a warm inhomogeneous plasma has been considered in general by Baldwin,[7] but the results of Gil'Denburg[3] for a specific density profile will be used here to study the field near the resonance point.

Consider the density profile shown in Fig. X-10. Under the assumption that the

wavelength of the electric field is much larger than the Debye length λ_D, a hydrodynamic formulation for the electric field can be used. This assumption is violated in the regions

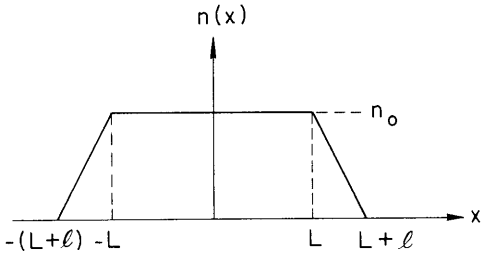

Fig. X-10. Inhomogeneous plasma slab.

of low density where the hydrodynamic description must be supplemented with results of kinetic theory.

The differential equation for the electric field E_1 inside the plama is[3]

$$\gamma \frac{v_{th}^2}{\omega^2} \frac{d^2E_1}{dx^2} + \left(1 - \frac{\omega_p^2}{\omega^2}\right) E_1 = E_{ext}, \tag{18}$$

where v_{th} is the average thermal velocity, and E_{ext} is the complex amplitude of the field outside ($|x| > L + \ell$) the plasma which is oscillating at frequency ω. The quantity γ is the constant in the equation of state used for the electron pressure, $p \sim n^{\gamma}$. Note from (18) that if v_{th} is zero, the cold plasma result is recovered.

The solution to (18) in the uniform region is

$$E_1 = \frac{E_{ext}}{1 - \frac{\omega_p^2}{\omega^2}} + C_1 \cosh k_o x, \tag{19}$$

where ω_{po} is the plasma frequency in the uniform region, and

$$k_o = \sqrt{\frac{\omega_{po}^2 - \omega^2}{\gamma v_{th}^2}}. \tag{20}$$

In obtaining (19), the antisymmetric solution, $\sinh k_o x$, was discarded, since the slab is driven by a symmetric external field. The constant C_1 is determined by connecting the solution in the tapered region to the uniform region solution at $x = \ell$ and requiring that E_1 and dE_1/dx be continuous there.

In the tapered region (using $(-L-\ell) < x < -L$ as an example), the solution to Eq. 18 is

$$E_1 = \sqrt{\pi}\, C_2[\mathrm{Bi}(z)-j\mathrm{Ai}(z)] + \pi a E_{ext}\left[\mathrm{Bi}(z)\int_{-\infty}^{z}\mathrm{Ai}(t)\,dt - \mathrm{Ai}(z)\int_{-\infty}^{z}\mathrm{Bi}(t)\,dt\right], \tag{21}$$

where

$$z = -a\left[\left(1-\frac{\omega_{po}^2}{\omega^2}\right) - \frac{\omega_{po}^2}{\omega^2}\,\frac{(L+x)}{\ell}\right] \tag{22a}$$

and

$$a = \omega^2\left[\frac{\ell}{\sqrt{\gamma}\, v_{th}\omega_{po}^2}\right]^{2/3}. \tag{22b}$$

The functions Ai and Bi are Airy functions of the first and second kind.[8] If the resonance point is in the tapered region, the first term that is the homogeneous solution in (21) can be shown to represent a "disturbance" propagating in the negative x direction toward the plasma boundary. The other homogeneous solution (which would represent a disturbance propagating in the +x direction) has been discarded because it could be excited only by a reflection at the plasma boundary. Gil'Denburg argued that the negative-traveling disturbance will be heavily Landau-damped in the region of low plasma density, and hence this reflected disturbance will not be excited. The second term in (21) represents the cold plasma solution far from the resonance point.

Connecting the two solutions (21) and (19) at x = -L determines[3] C_1 and C_2. The field near the resonance point (z = 0) in the limit of small thermal velocity[3] then becomes

$$\frac{E}{E_{ext}} \approx \frac{\omega_p^2}{\left[v_{th}\left(\omega_p^2\right)'\right]^{2/3}}, \tag{23}$$

while the electron density goes as

$$\frac{en_1}{\epsilon_o E_{ext}} \approx \frac{\left(\omega_p^2\right)'\omega_p^2}{\left[v_{th}\left(\omega_p^2\right)'\right]^{4/3}}, \tag{24}$$

The time average power flow in the plasma disturbance that propagates away from the resonance point agrees with the result given in Eq. 11 in the limit of zero thermal velocity.

Impedance of the Inhomogeneous Plasma

The transient response of an inhomogeneous plasma reported previously[9] may be used to find the steady-state impedance of an inhomogeneous plasma placed between two capacitor plates as shown in Fig. X-11. The plates are assumed to be located where the plasma density vanishes.

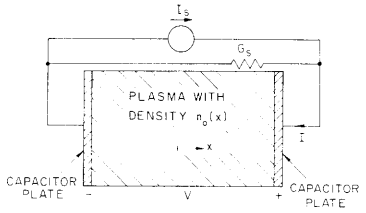

Fig. X-11. Inhomogeneous plasma between a pair of capacitor plates.

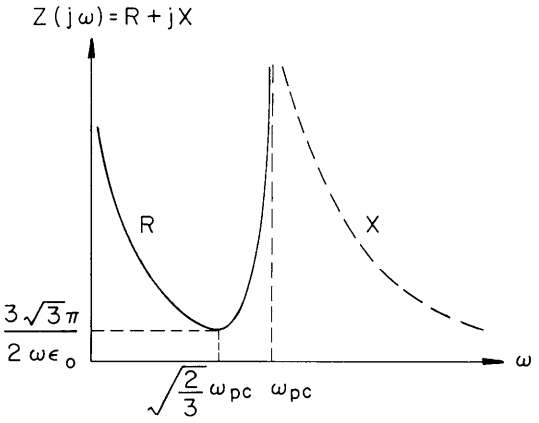

Fig. X-12. Impedance of the plasma-filled capacitor.

Using the fact that for a plasma placed between a pair of plates the uniform displacement perturbation at t = 0 corresponds to a capacitor current excitation which is a triplet function of time, the relation between the capacitor current and particle displacement is

$$I(s) = \left(\frac{\epsilon_o m \delta}{e}\right) s^2, \tag{25}$$

where s is the Laplace transform variable. The voltage response of the plasma[9] is

$$V(s) = -\frac{se\delta}{\epsilon_o} \int_{-\infty}^{\infty} \frac{n_o(x)\, dx}{s^2 + \omega_p^2(x)}, \tag{26}$$

so the impedance Z(s) = V(s)/I(s) becomes

$$Z(s) = -\frac{1}{s\epsilon_o} \int_{-\infty}^{\infty} \frac{\omega_p^2(x)\, dx}{s^2 + \omega_p^2(x)}. \tag{27}$$

For the general class of density functions $n_o(x) = n_c/(1+x^{2k})$, the impedance is

$$Z(j\omega) = -\frac{\omega_{pc}^2}{\epsilon_o}\frac{\pi}{k \sin\frac{\pi}{2k}}\frac{1}{(j\omega)^{(1+1/k)}(\omega_{pc}^2-\omega^2)^{(1-1/2k)}}, \tag{28}$$

where we have written $s = j\omega$. As an example, consider the case $k = 1$, a plasma with density $n_o = n_c/(1+x^2)$. The impedance becomes

$$Z(j\omega) = \frac{\pi}{\epsilon_o}\frac{\omega_{pc}^2}{\omega^2}\frac{1}{\sqrt{\omega_{pc}^2 - \omega^2}}, \tag{29}$$

which is sketched in Fig. X-12. Note that for $\omega < \omega_{pc}$ the impedance is pure real; one would calculate the power dissipated as

$$P = \frac{1}{2}\frac{\pi}{\epsilon_o}\frac{\omega_{pc}^2}{\omega^2}\frac{|I|^2}{\sqrt{\omega_{pc}^2 - \omega^2}}. \tag{30}$$

Using the relation between the circuit current and the electric field at the plates, $I = -j\omega\epsilon_o E_{ext}$, the power dissipated becomes

$$P = \frac{1}{2}\pi\epsilon_o\omega_{pc}^2\frac{|E_{ext}|^2}{\sqrt{\omega_{pc}^2 - \omega^2}}. \tag{31}$$

This result, obtained from the impedance formulation of the cold plasma can be shown to agree exactly with the expressions for power dissipated in an inhomogeneous plasma in the limit of zero collision frequency or zero thermal velocity.

Finally, note that the singularity in the power dissipated at $\omega = \omega_{pc}$ (Eqs. 30 and 31) is a consequence of using the current I to the plates, which is not constant with frequency if a nonideal source such as that shown in Fig. X-11 is used. In fact, the current I in this case is given by

$$I = \frac{I_s}{1 + ZG_s}, \tag{32}$$

where G_s is the source conductance, and Z is the plasma impedance. The power dissipated in the plasma in terms of the source current I_s (for $Z = R$) becomes

$$P = \frac{R|I_s|^2}{(1+RG_s)^2}, \tag{33}$$

which remains finite for all R as long as G_s is nonzero.

H. M. Schneider, A. Bers

References

1. H. M. Schneider, Quarterly Progress Report No. 84, Research Laboratory of Electronics, M.I.T., January 15, 1967, p. 149.
2. H. M. Schneider, Quarterly Progress Report No. 89, Research Laboratory of Electronics, M.I.T., April 15, 1968, p. 127.
3. V. B. Gil'Denburg, Soviet Phys. – JETP 18, 5 (May 1964).
4. R. J. Briggs and S. F. Paik, Int. J. Electronics 23, 2 (1968).
5. W. P. Allis, S. J. Buchsbaum, and A. Bers, Waves in Anisotropic Plasmas (The M.I.T. Press, Cambridge, Mass., 1963).
6. B. D. Fried and S. D. Conte, The Plasma Dispersion Function (Academic Press, Inc., New York, 1961).
7. D. E. Baldwin (Private communication, 1968).
8. M. Abramowitz and I. A. Stegun, Handbook of Mathematical Functions (Dover Publications, New York, 1965).
9. A. Bers and H. M. Schneider, Quarterly Progress Report No. 89, op. cit., p. 123.

X. PLASMAS AND CONTROLLED NUCLEAR FUSION

B. Applied Plasma Physics Related to Controlled Nuclear Fusion*

Academic and Research Staff

Prof. T. H. Dupree
Prof. E. P. Gyftopoulos
Prof. L. M. Lidsky
Prof. N. L. Oleson
Prof. T. O. Ziebold
Dr. R. A. Blanken

Graduate Students

D. G. Colombant
R. E. Fancher
M. Hudis
M. A. Le Comte
G. R. Odette
C. E. Wagner

1. HIGH INTENSITY 14-MeV NEUTRON SOURCE

We are studying a new design for a 14-MeV neutron source with $10^{14}/cm^2$-sec surface flux. (See Fig. X-13.) The key feature is the use of the Mach line of a freely expanding deuterium gas jet as the target for a high-energy tritium ion beam. The neutrons are produced by the D-T fusion reaction. The density gradient at the Mach line serves as a "windowless" target, while the energy deposited by the tritium beam (~200 kW in this design) is removed from the small interaction region by the flowing gas stream. The beam energy is eventually removed from the system far downstream of the reaction zone in a region of much larger surface area.

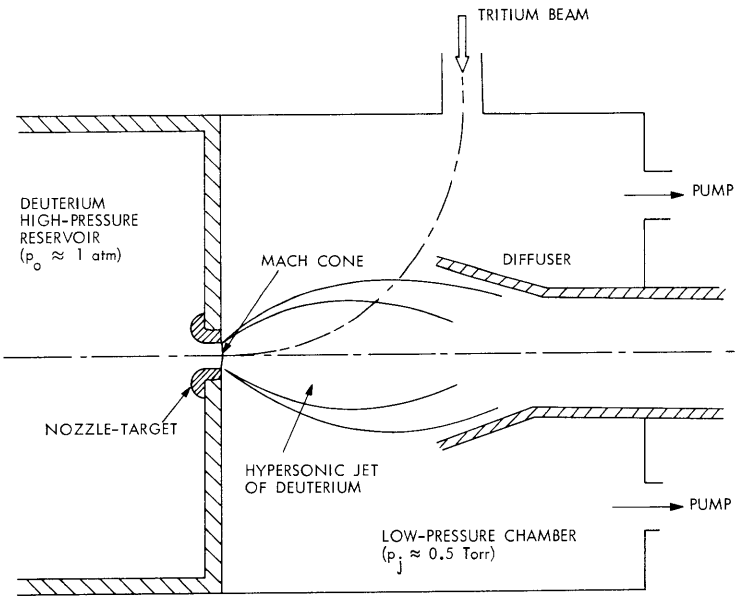

Fig. X-13. Conceptual scheme of the high-intensity neutron source.

*This work was supported by the National Science Foundation (Grant GK-2581).

The detailed properties of the unperturbed gas flow are known. Our goal now is to gain an understanding of how the flow properties are modified by strong local heating, especially in the transonic interaction region. A full description of the interaction requires the solution of the full set of gasdynamics equations in two dimensions coupled to the range-energy relation describing the slowing down of the tritium beam. The difficulties associated with this problem are the following.

1. The system of equations is nonlinear not only in the usual sense of gasdynamics but also in the interaction between the deuterium and tritium flows.
2. The free-boundary problem for the D_2 jet.
3. The boundary conditions are given upstream for the deuterium (reservoir conditions) and downstream for the tritium (energy, intensity of the beam).
4. The zone of strongest interaction is located at the position where the Mach number passes through unity. The flow behavior changes radically at this point.
5. The stability of the flow to small perturbations is not known. This requires the solution of an auxiliary time-dependent set of equations to determine the transient behavior.

Steady-State Solution

Because of the many problems involved, we have chosen to solve a simplified model first. The results of a one-dimensional, time-independent treatment will be described here. For this case, the system of equations to be solved is

$$\rho A u = C_1 \tag{1}$$

$$\rho u \frac{du}{dx} = -\frac{dp}{dx} \tag{2}$$

$$\rho c_p u \frac{dT}{dx} + \rho u^2 \frac{du}{dx} = \frac{I_T \rho}{A V_T^2} \ln \left(C_2 V_T^2 \right) \tag{3}$$

$$p = \rho R T \tag{4}$$

$$M_T V_T \frac{dV_T}{dx} = \frac{B\rho}{V_T^2} \ln \left(C_2 V_T^2 \right), \tag{5}$$

where the subscript "T" refers to the tritium beam, and B, C_1, C_2 are constants. Equations 1-3 are simply the moment equations of gas flow in conventional notation. The term on the right-hand side of the energy equation describes the D-T energy exchange (the momentum of the tritium beam is negligible). Equation 4 is an adequate equation of state for the moderate-temperature, moderate-density deuterium jet, and Eq. 5 describes the slowing of the tritium ion beam on the neutral gas. The approximations made in deriving

Eq. 5 break down below 20 keV ion energy, but only 10% of the initial beam energy remains and the D-T reaction rate is almost completely negligible. We neglect the D-T interaction below 20 keV in the present solution.

A typical solution, as well as a comparison with a case without tritium, is shown in Fig. X-14. Both solutions have the same conditions at the sonic line (computations were

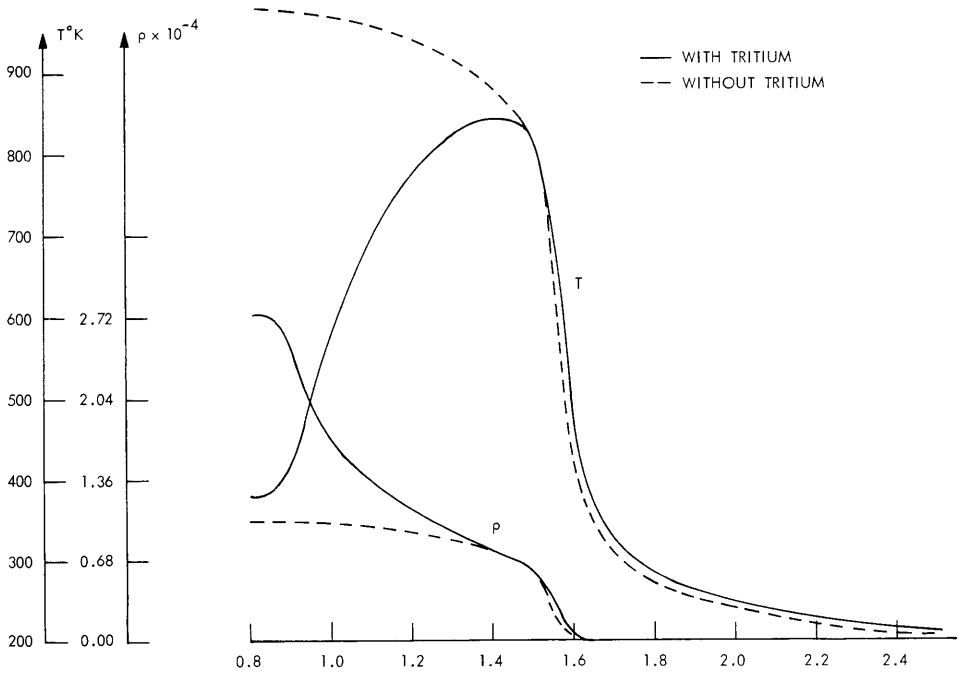

Fig. X-14. Comparison of flow patterns with and without tritium for the same sonic conditions and nozzle.

started from this line) and take place in the same geometry (same nozzle and free expansion). The flattening of the upstream conditions for the tritium case occurs when the tritium energy has reached 20 keV; that is, when the tritium deuterium interaction is assumed to vanish. The maximum temperature in the nozzle is only approximately 850°K. This choice led to a rather large deuterium mass flow rate (32 g/sec) but, on the other hand, it did not introduce complications as far as dissociation of D_2 was concerned. The main feature of these curves is, however, that the density gradient in the transonic region is almost as sharp in both cases.

Time-Dependent Solution

(i) System of Equations

First, we note that the tritium velocity is 3-4 orders of magnitude greater than the deuterium velocity, and so we do not need to include the tritium dynamics in a

time-dependent solution for the deuterium flow field.

In a variable cross-section geometry, the complete equations for the deuterium dynamics read:

$$\frac{\partial \rho}{\partial t} + \frac{\partial}{\partial x}(\rho u) + \rho u \frac{1}{A}\frac{dA}{dx} = 0 \tag{6}$$

$$\frac{\partial}{\partial t}(\rho u) + \frac{\partial}{\partial x}(\rho u^2 + p) + \rho u^2 \frac{1}{A}\frac{dA}{dx} = 0 \tag{7}$$

$$\frac{\partial}{\partial t}\left[\rho\left(e + \frac{1}{2}u^2\right)\right] + \frac{\partial}{\partial x}\left[\rho u\left(e + \frac{1}{2}u^2\right) + pu\right] + \left[\rho u\left(e + \frac{1}{2}u^2\right) + pu\right]\frac{1}{A}\frac{dA}{dx} = \frac{I_T \rho}{AV_T^2}\ln\left(CV_T^2\right) \tag{8}$$

$$p = \rho R T \tag{9}$$

to which the energy range relationship for the tritium must be added:

$$m_T v_T \frac{dV_T}{dx} = \frac{B\rho}{V_T^2}\ln\left(CV_T^2\right). \tag{10}$$

In Eqs. 6-8, A has been assumed to be independent of time (that is, the assumption is made that the tritium does not bring any change in the boundaries).

At this point it is interesting to take as new variables the physical quantities ρ, $\rho u \equiv M$, $\rho\left(e + \frac{1}{2}u^2\right) \equiv E$. Besides the obvious advantage of expressing the conservation laws in their simplest forms, they lend themselves readily to a powerful treatment of shocks. These variables were first used by Lax.[1]

Defining $R = (\gamma-1)E + \frac{(3-\gamma)}{2}\frac{M^2}{\rho}$, $T = \frac{\gamma E M}{\rho} - \frac{(\gamma-1)}{2}\frac{M^3}{\rho^2}$, we can rewrite the system above in the following form:

$$\frac{\partial \rho}{\partial t} + \frac{\partial M}{\partial x} + \frac{M}{A}\frac{dA}{dx} = 0 \tag{11}$$

$$\frac{\partial M}{\partial t} + \frac{\partial R}{\partial x} + \frac{M^2}{\rho}\frac{1}{A}\frac{dA}{dx} = 0 \tag{12}$$

$$\frac{\partial E}{\partial t} + \frac{\partial T}{\partial x} + T\frac{1}{A}\frac{dA}{dx} = \frac{I_T \rho}{AV_T^2}\ln\left(CV_T^2\right) \tag{13}$$

$$m_T v_T \frac{dV_T}{dx} = \frac{B\rho}{V_T^2}\ln\left(CV_T^2\right). \tag{14}$$

It can be shown that this system is hyperbolic and that some care must be taken in

choosing the boundary conditions. A well-posed problem needs only to have the boundary values (ρ, M, E) specified at the origin, x_o, plus a complete set of initial values at $t = 0$, the boundary condition remaining at x_L for the tritium velocity. The specification of some boundary values at an extra point would almost necessarily lead to an ill-posed problem. This can be seen best in the supersonic part of the flow where upstream propagation cannot occur.

To ensure nearly correct treatment of shocks (thermal shocks are expected), the following "viscosity" terms will be introduced in the previous system of equations. Since they have the same form for the first three equations, we shall consider only the first one. In finite difference form the first term will be written

$$\frac{1}{\delta t}\left[\rho_{i,j+1} - \frac{k}{2}(\rho_{i+1,j}+\rho_{i-1,j}) + (k-1)\rho_{i,j}\right], \tag{15}$$

where i is the space index, and j the time index. Expression (15) can be rewritten

$$\frac{1}{\delta t}\left[(\rho_{i,j+1}-\rho_{i,j}) - \frac{k(\delta x)^2}{2}\,\frac{(\rho_{i+1,j}-2\rho_{i,j}+\rho_{i-1,j})}{(\delta x)^2}\right]. \tag{16}$$

This expression is, in fact, the finite difference form of the following terms:

$$\frac{\partial \rho}{\partial t} - D\frac{\partial^2 \rho}{\partial x^2}, \tag{17}$$

where $D = \dfrac{k(\delta x)^2}{2\delta t}$.

Substituting terms of the form (17) in the system (Eqs. 11-13), we get:

$$\frac{\partial \rho}{\partial t} + \frac{\partial M}{\partial x} + \frac{M}{A}\frac{dA}{dx} - D\frac{\partial^2 \rho}{\partial x^2} = 0 \tag{18}$$

$$\frac{\partial M}{\partial t} + \frac{\partial R}{\partial x} + \frac{M^2}{\rho}\frac{1}{A}\frac{dA}{dx} - D\frac{\partial^2 M}{\partial x^2} = 0 \tag{19}$$

$$\frac{\partial E}{\partial t} + \frac{\partial T}{\partial x} + \frac{T}{A}\frac{dA}{dx} - D\frac{\partial^2 E}{\partial x^2} = \frac{I_T \rho}{AV_T^2}\ln\left(CV_T^2\right). \tag{20}$$

This system can be rewritten in more conventional variables:

$$\frac{\partial \rho}{\partial t} + \frac{\partial}{\partial x}(\rho u + m) + \frac{\rho u}{A}\frac{dA}{dx} = 0 \tag{21}$$

$$\frac{\partial(\rho u)}{\partial t} + \frac{\partial}{\partial x}\left[p+q+u(\rho u+m)\right] + \rho u^2 \frac{1}{A}\frac{dA}{dx} = 0 \tag{22}$$

$$\frac{\partial}{\partial t}\left[\rho\left(e+\frac{1}{2}u^2\right)\right] + \frac{\partial}{\partial x}\left[u(p+q) + (pu+m)\left(e+\frac{1}{2}u^2\right)+h\right]$$

$$+\left[\rho u\left(e+\frac{1}{2}u^2\right)+pu\right]\frac{1}{A}\frac{dA}{dx} = \frac{I_T\rho}{AV_T^2}\ln\left(CV_T^2\right) \tag{23}$$

$$p = \rho RT, \tag{24}$$

where

$$m = -D\frac{\partial\rho}{\partial x}$$

$$q = -D\rho\frac{\partial u}{\partial x}$$

$$h = -D\rho\frac{\partial e}{\partial x}$$

play the roles of mass diffusion, viscosity, and heat-conduction terms. Varying k controls the influence of these effects, and setting k = 0 gives back the original equations.

(ii) Computational Scheme

Because of the two different time scales involved in this problem, it is evident that the tritium velocity distribution will be obtained at once at the end of every time step of the computations of the deuterium flow field, by a backward integration of the energy-range relationship. So we shall not emphasize this point, but rather concentrate on the equations governing the deuterium flow.

Our aim is to solve the equations for the whole transients and to see how they reach the steady state. Since the time involved might be several transit times, we are interested in maximizing the size of the time step used in the computations. This goal has led us to an extensive study of different schemes and algorithms. The first physical limitation to the size of the time step is the fact that one cannot follow the motion of a perturbation in the flow at intervals of time greater than the time it takes for the perturbation to be carried one space-step away. This condition, namely $\tau = \Delta t \lesssim \frac{\Delta x}{|u+c|}$, is the stability condition of standard hyperbolic schemes (c = speed of sound); however, it has been known for some time that implicit schemes allow the easing of this restriction. The idea is to use in the computation the values of the terms which do not contain the time explicitly at both ends of the time step considered. For example, (6) in finite difference form will be written

$$\frac{(\rho_{i,j+1}-\rho_{i,j})}{\delta t} + \lambda\left[\frac{1}{2\delta x}(M_{i+1,j+1}-M_{i-1,j+1}) + M_{i,j+1}\left(\frac{1}{A}\frac{dA}{dx}\right)_i\right]$$

$$+ (1-\lambda)\left[\frac{1}{2\delta x}(M_{i+1,j}-M_{i-1,j}) + M_{i,j}\left(\frac{1}{A}\frac{dA}{dx}\right)_i\right] = 0, \qquad (25)$$

where λ = implicit factor ($\lambda = 0$ is called explicit). The stability of this scheme is still not known in general.

Several comments about this scheme might be made at this point. The choice of the central-difference scheme for the gradient operator is essential to produce the implicit scheme. Any backward or forward difference scheme coupled to the boundary conditions at the origin leads to an explicit formulation and to its restrictive stability condition. Moreover, the central difference scheme requires the specification of other boundary conditions, since we now have a system of $3 \times (N-2)$ equations for $(3N-3)$ unknowns (N is the number of spatial points used in the computations). We have discussed the addition of another boundary condition to the problem and seen that it was not desirable. This seems to be the price, however, for using the implicit scheme. We can be guided in our choice by the steady-state solution. Since the solution of the equations that we are trying to solve will eventually reach steady-state conditions, and there is practically no interaction between tritium and deuterium beyond Mach number 3 or more, we shall take some value of the far downstream steady-state solution obtained previously as new boundary conditions. It should be remembered that this boundary should never be adjusted later on because this would mean propagation upstream in the supersonic part of the flow.

These ideas have been tested on real cases, at first, involving no tritium, to find out what size of time step could be used. We started with a steady-state condition, and a time evolution of these conditions was sought. For every time step, iterations were performed until convergence was obtained. We first realized that, because of the large spatial gradients in the problem, Δx had to be chosen rather small. $\Delta x = 0.0125$ cm was adopted for the following series of tests. This choice is in itself a restriction for the absolute value of Δt, since it is proportional to Δx, but we are more interested in discussing the relative advantages of implicit schemes over explicit ones.

Very soon the scheme described above produced instabilities either when iterations were continued after convergence had been achieved or when several time steps were computed. The explicit scheme seemed to be more stable as far as the iterations were concerned, but broke down much earlier when the time was increased. All instabilities observed took place in the subsonic part of the flow. Subsonic and supersonic parts of the flow were then tested separately. Values of 100τ could be used as time steps in the supersonic region without producing any instability, whereas values of a few τ only could be used in the subsonic part. The complete central-difference scheme developed

instabilities first at the lowest Mach numbers. Their growth rate was very large (2 or 3 time steps or iterations would be sufficient to make one of the variables become negative), and their wavelength was of the order of a few space steps.

Other schemes were tried which combined the central-difference scheme and the backward/forward difference schemes as suggested by R. Lelevier,[2] the idea being to transport one quantity throughout the flow. These schemes proved unstable too, but at Mach numbers close to unity, their growth rate was smaller than for complete central-difference schemes, as well as the wavelength of the instabilities.

Finally, a predictor-corrector scheme was tried as suggested by Gourlay and Morris.[3] This scheme proved unstable both for Mach numbers low and nearly equal to 1.

In order to try to damp out these instabilities, viscosity, as described above, was included in the equations. Not much improvement was observed. From these tests, it seems that the practical limitation on Δt has to be of the order of a few τ and, since the instabilities are growing fast enough, the solution will not deviate for a long time before the computations are stopped automatically. Some initial perturbation to the steady-state conditions was then included to constitute a second series of tests. Few conclusions from these runs differ appreciably from the previous ones. We noticed, however, that the viscosity worked effectively in bringing back the steady state, and it seemed that during these transients Δt could be increased to 5τ without affecting the precision of the solution.

In conclusion, it might very well be that the low stability condition of these schemes is due to the overdeterminations. This fact has been discussed at some length by Parter.[4] Even if the extra boundary value is the right one, it will not be exactly compatible with the set of finite-difference equations, and an error will be introduced and propagated in the solution.

D. Colombant, L. M. Lidsky

References

1. P. D. Lax, Communs. Pure Appl. Math. 7, 159 (1954).
2. R. Lelevier, quoted in R. D. Richtmeyer, Difference Methods for Initial Value Problems (1957), p. 194.
3. A. R. Gourlay and J. L. Morris, Math. Comp. 22, 28 (1968).
4. S. V. Parter, Num. Math. 4, 277 (1962).

2. PARTICLE FLUX MEASUREMENTS IN A HOLLOW-CATHODE ARC

Introduction

The relation between enhanced plasma transport and observed oscillation spectra is complicated and, in fact, still confusing. The magnitude of the enhanced plasma transport attributable to a finite-amplitude instability cannot usually be deduced from linearized calculations. A rigorous nonlinear theory of induced plasma losses predicting experimental amplitudes and phase difference has not been reported. There is still need for experimental data.

Indirect measurements of classical and enhanced radial fluxes are complicated by specific problems, for example, the separation of fluxes from other losses such as charge exchange, DC drifts, volume or end plate recombination. Direct measurements of these fluxes are also complicated, because of the small velocities involved, the changes in local plasma density and its gradient in the presence of probes. Thus far, measurements of radial fluxes in experimentally produced plasmas have all been measured by using indirect methods. We propose to measure the radial particle flux in a hollow-cathode arc by a direct method. Investigation of the experimental method and preliminary radial flux measurements will be presented and discussed in this report.

One-sided Langmuir probes rotating about their axes were used to measure radial fluxes (see Figs. X-15 and X-16). The major effect of a drifting distribution function on ion-saturation current for a nonsymmetrical probe was isolated for the range of probe plasma parameters in our experiment. The magnitude of this change was related to the average velocity of the drifting particles.

Preliminary results of measured radial fluxes have demonstrated that this method is sensitive enough to distinguish between enhanced and collisional radial fluxes. Although it is too early to draw definite conclusions, there is strong indication that diffusion over a defined range of plasma parameters is related to the ion enrichment in the anode sheath.

Probe Work

Probe theory has been developed for symmetrical probes in a plasma with no magnetic field. In the case of a magnetic field, $\rho_i/R > 1$, where ρ_i is the gyro radius, and R is the probe plus insulator radius, it has been shown experimentally that ion saturation current and the transition region current are described by nonmagnetic field probe theory. Probe theory for ion-saturation current takes two different forms, depending on whether $R/\lambda_d^- > 1$ or $R/\lambda_d^- < 1$, where λ_d^- is the electron Debye length.[1] For the case $R/\lambda_d^- > 1$, theory tells one to expect nonorbital motion with a sheath thickness $\ll R$. For the case $R/\lambda_d^- < 1$, theory tells one to expect orbital motion with a sheath thickness $\gg R$.

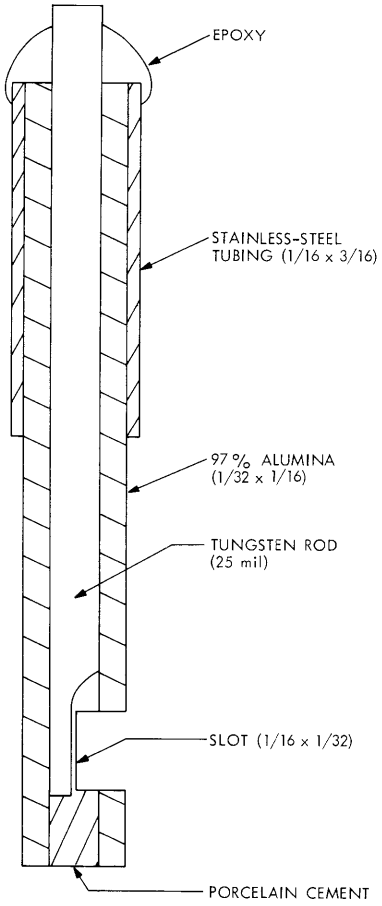

Fig. X-15. Langmuir probes for measuring radial fluxes.

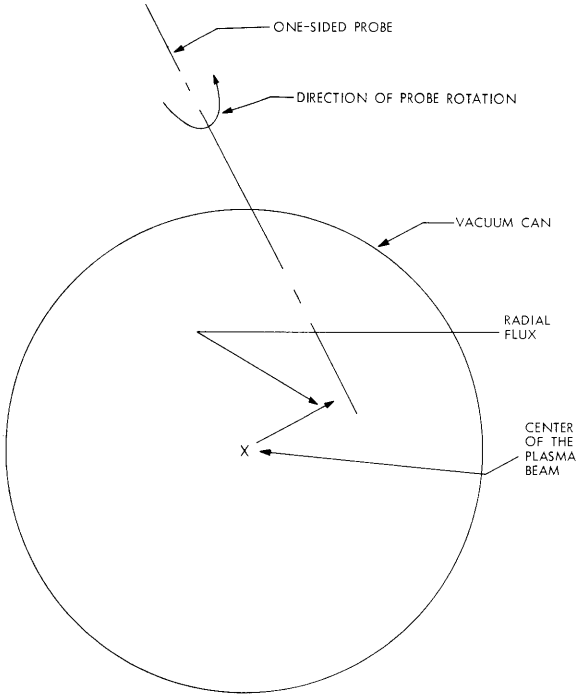

Fig. X-16. Cross section of the vacuum can as seen by looking from cathode to anode.

The probe work was restricted to the following range of parameters: $\lambda > \rho_i > R > \lambda_d^-$, $R/\lambda_d^- \geq 40$, $T_i/T_e \cong 0.1$, $\rho_i/R > 3$, where λ is the collision mean-free path, T_e and T_i are the electron and ion temperatures. The operating conditions in the hollow-cathode arc[2] establish the probe parameters listed above.

The theory for ion-saturation currents measured by symmetrical probes within the described range of parameters predicts[3]

$$I_s^i = I_s^i\left[R/\lambda_d^-, T_i/T_e, q(\phi_p-\phi_s)/kT_e \right],$$

where I_s^i is the ion-saturation current, ϕ_p and ϕ_s are the probe and space potentials. Ion-saturation current is affected by three physical processes that are described by the functional dependence of I_s^i on R/λ_d^-, T_i/T_e, and $q(\phi_p-\phi_s)/kT_e$. The total sheath thickness is a measure of how far into the plasma the probe can affect particle motion. Conservation of orbital angular momentum describes the probability that a particle will be collected, provided that the particle falls within the region of probe influence. The sheath condition on the ion velocity at the sheath edge describes the drop in potential across the quasi-neutral region and corresponds to the drop in density through this region. For $T_i/T_e \leq 0.1$, it has been demonstrated that conservation of orbital angular momentum is a secondary effect and can be neglected. For $T_i < T_e$, the ions must have a velocity $\sqrt{kT_e/M_i}$ at the sheath edge in order to satisfy the boundary conditions between the sheath's edge and the quasi-neutral region. For $R/\lambda_d^- > 40$ but < 150, the effect of finite sheath thickness can be bounded by a factor of two, and therefore represents an important effect. Because $T_i \approx 0.1\ T_e$, the drop in density through the quasi-neutral region is also an important factor.

The response of a nonsymmetrical probe is usually estimated by scaling through the ratio of areas to the response of a symmetrical probe. Experimental work conducted with both symmetrical and nonsymmetrical probes within the range of parameters described above, has demonstrated the following:

1. The response of different shaped probes does not scale with area.

2. The response of individual probes to local changes in the plasma when normalized to some arbitrary state, scales almost one for one.

Therefore we conclude that nonsymmetrical and symmetrical probes respond in the same fashion when subjected to the same local plasma conditions.

Adding a drift velocity to the particle's velocity distribution for a plasma changes the response of a symmetrical probe by either affecting the total sheath thickness or the potential drop across the quasi-neutral region. Provided that the drifting velocity is $\leq \sqrt{kT_e/M_i}$, it can be shown that the sheath thickness – not including the quasi-neutral region – is unaffected by the drifting velocity. The density drop through the quasi-neutral region is affected by the drift, and causes either an increase or decrease in the

saturation current (on a scale of $e^{\pm(u_i/u_o)^2}$, where u_i is the ion drifting velocity, and $v_o = \sqrt{2kT_e/M_i}$). These results have been verified by comparing the response of a one-sided probe facing upstream and downstream from the drift to the response of a spherical probe. Using these ideas along with Bohn's[4] sheath condition and Langmuir's[5] space-charge-limited current equation to estimate the sheath thickness, one finds the following relationship:

$$\Delta I_s^i = qA\left(1+\frac{D^2}{A}\right)N_\infty \frac{v_o e^{-1/2}}{\sqrt{2}}\left\{e^{(u_i/u_o)^2} - e^{-(u_i/u_o)^2}\right\}, \tag{1}$$

where

$$\frac{D^2}{A} = 4.98\,\frac{\left(\lambda_d^-\right)^2}{A}\,\psi_p\left(\psi_p^{1/2}+0.8\right), \qquad \psi_p = q\phi_p/kT_e.$$

Here, ΔI_s^i is the change in ion-saturation current seen by a one-sided probe looking upstream and downstream. Therefore, by measuring ΔI_s^i, T_e, and N_∞, one can find the magnitude of the drifting velocity.

Equation 1 was checked by using it to measure the azimuthal drift velocity caused by the E (radial electric field) × B drift. The direction of E predicted by Eq. 1 was found to be in good agreement with results predicted on similar machines by other people using different methods.[6] The magnitude was also found to be in good agreement.

Diffusion Experiment

The radial flux was measured by a one-sided probe rotating about its axis and associated equipment (see Fig. X-17). The reference signal is provided by a continuous rotatable sine-cosine potentiometer, and therefore provides a sinusoidal signal at the frequency at which the probe is being rotated. The reference signal and modulated ion saturation current were recorded on a visicorder. The fast operational amplifier is used as a gating amplifier, with the gate voltage provided by the timing circuit of the boxcar integrator. The boxcar integrator is triggered by the reference signal. The output from the gated operational amplifier has an AC amplitude at the rotating probe frequency which is proportional to the difference in ion saturation current. The magnitude of the

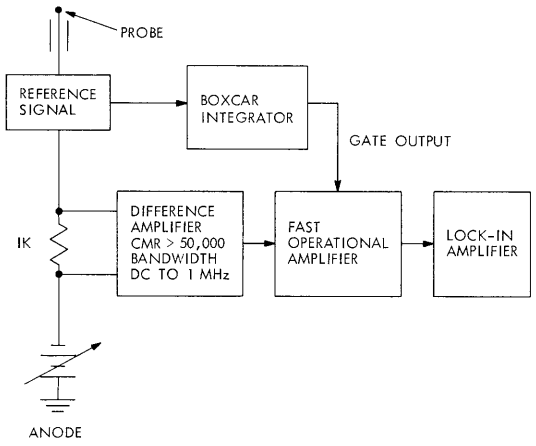

Fig. X-17. Diagram of the diffusion experiment.

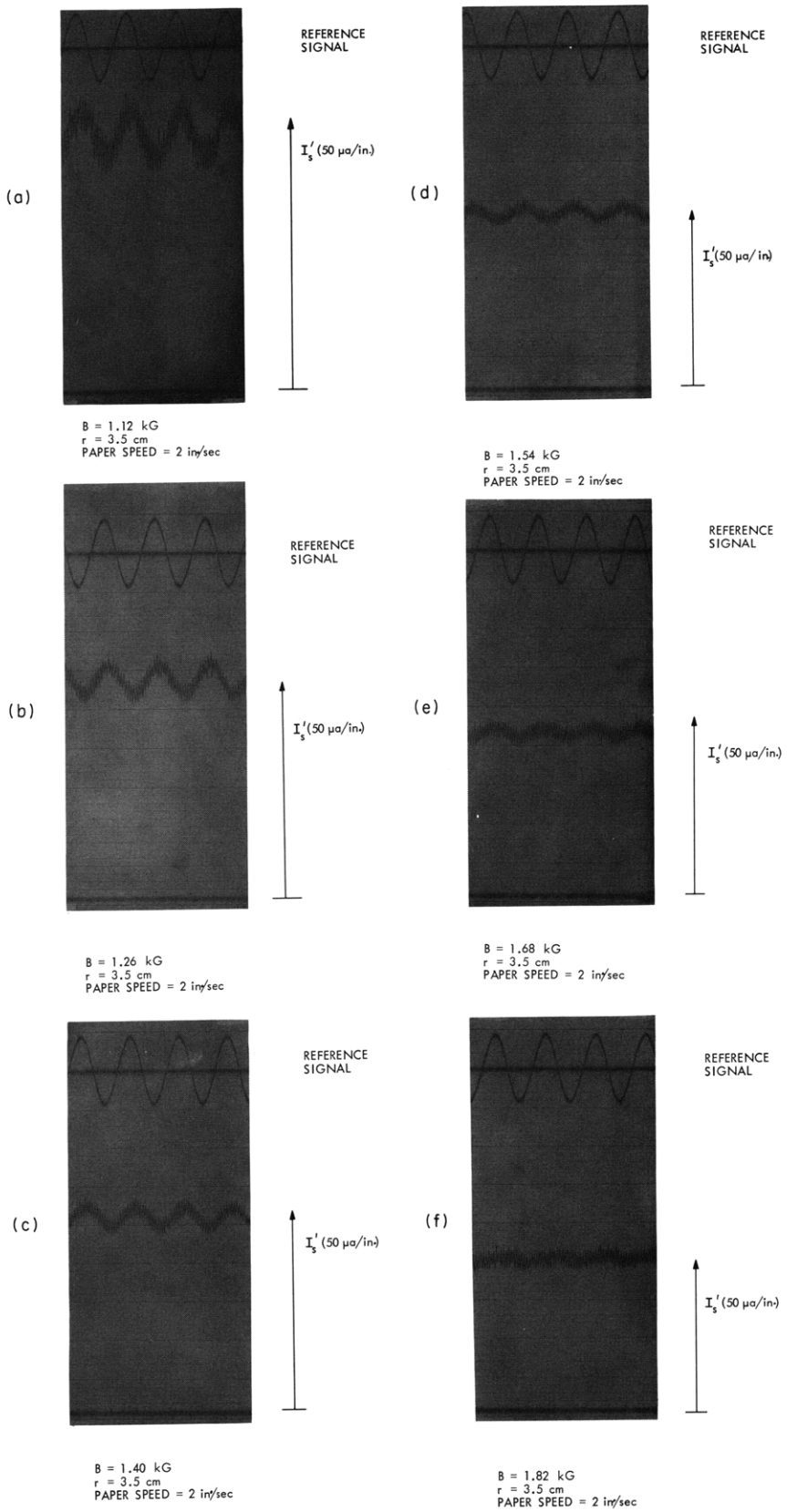

Fig. X-18. Results of measurements with the rotating one-sided probe.

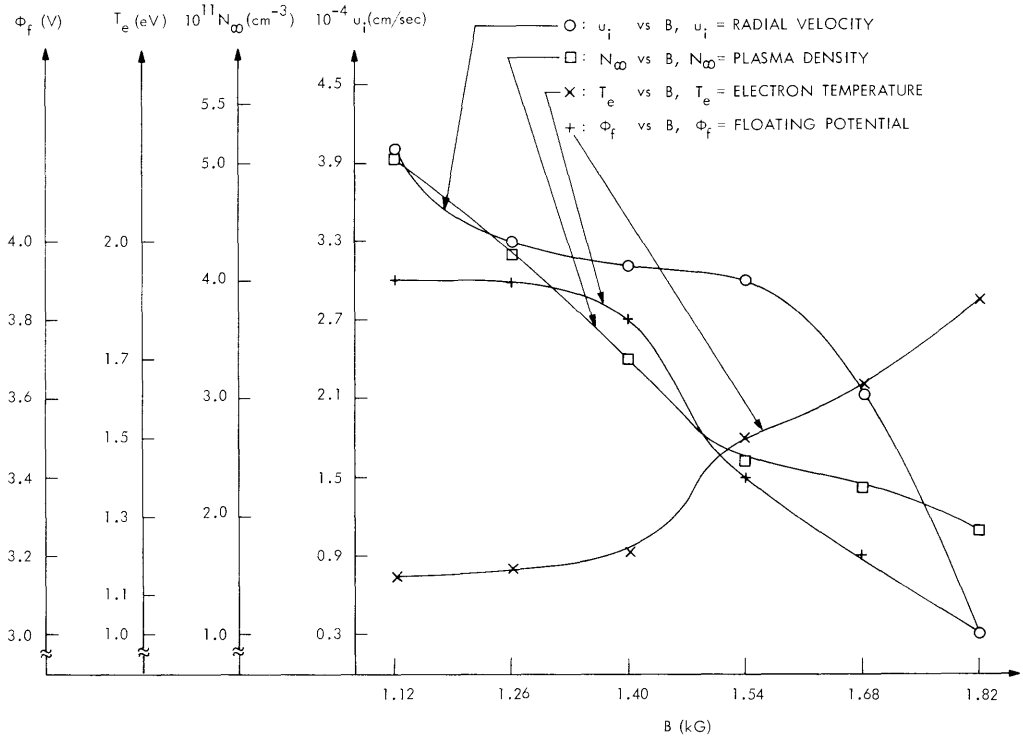

Fig. X-19. Radial flux vs magnetic field.

AC component was measured by using a lock-in amplifier. A typical modulated ion saturation current response measured by the rotating one-sided probe can be seen in Fig. X-18.

The following are some preliminary results of the radial flux, together with other plasma parameters. Figure X-19 shows the radial flux as a function of magnetic field. Also shown is density, temperature, and floating potential as a function of magnetic field. Figure X-20 shows potential and density fluctuations as a function of magnetic field, together with the current drawn by a grounded cylindrical probe (see Fig. X-21). The source field (field in the region where the plasma is produced) was kept constant at the value producing the most quiescent plasma. The radial position of the probe was kept constant at 3.5 cm.

Some interesting observations can be drawn from Figs. X-19 and X-20.

1. The radial flux decreased by almost an order of magnitude for a 20% change in magnetic field.

2. Density, floating potential and temperature remained almost constant over the same range of B.

3. For B between 1.35 kG and 1.54 kG, the radial flux, potential, and density fluctuations remained almost constant.

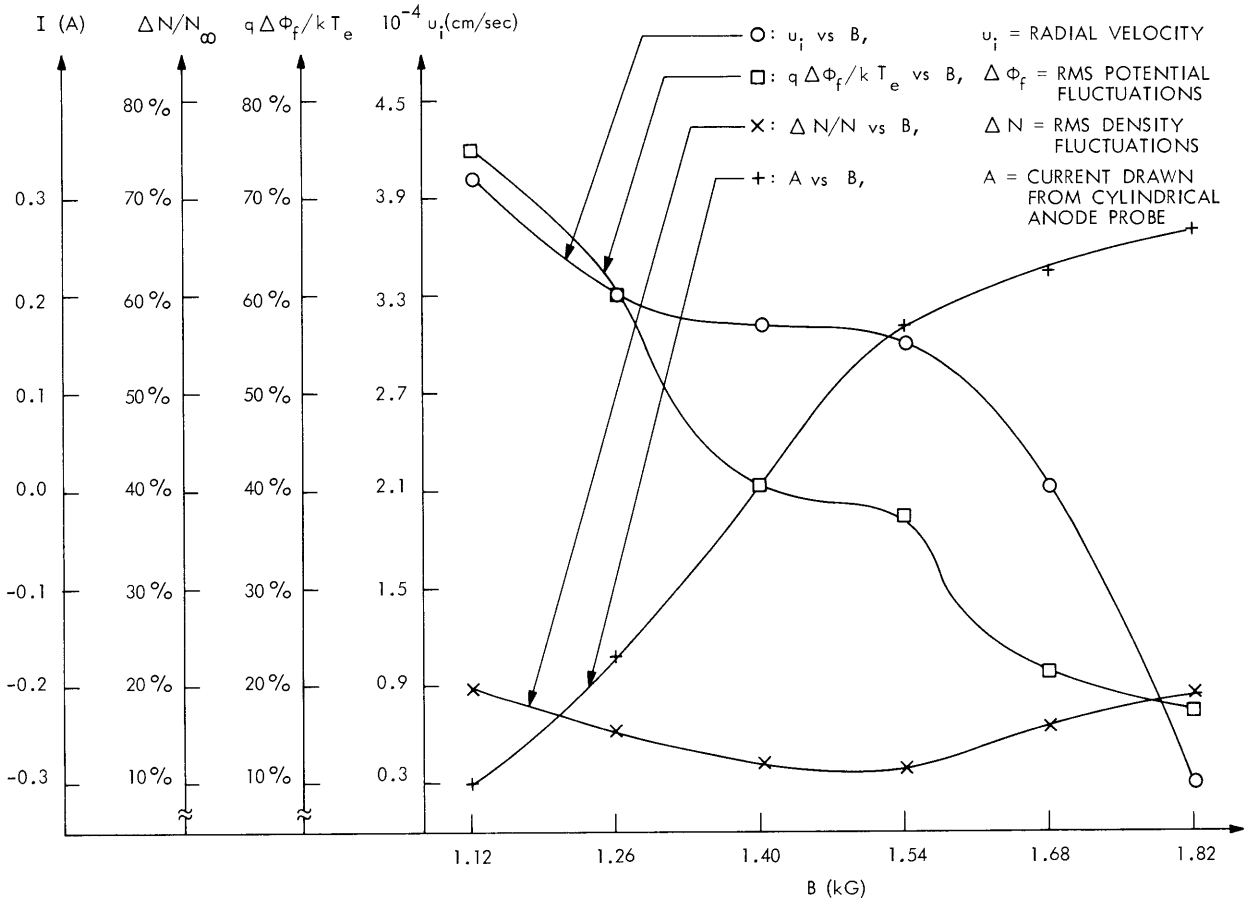

Fig. X-20. Potential and density fluctuations vs magnetic field.

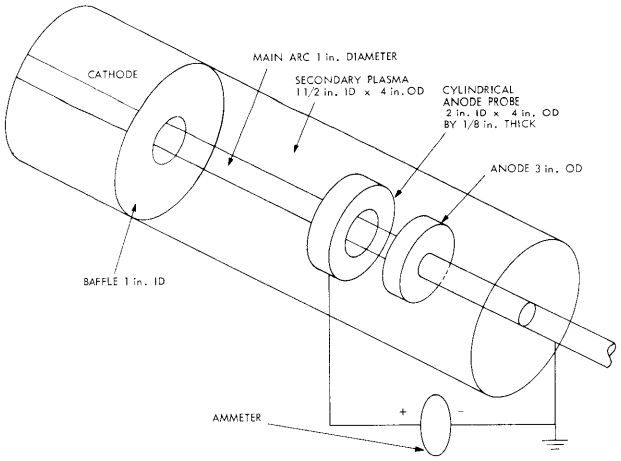

Fig. X-21. Grounded cylindrical probe.

4. At B = 1.5 kG the radial flux, potential, and density fluctuations underwent an abrupt change in magnitude.

5. The slope of density versus magnetic field changed abruptly at the same value of B.

A simple calculation suggests that for $\phi_f \geq +3$ V, the anode sheath becomes ion-enriched, while for $\phi_f \leq +3$ V, the anode sheath becomes electron-enriched. The anode wall probe indicates that the sheath is ion-enriched for $B \leq 1.5$ kG, but is electron-enriched for $B \geq 1.5$ kG. This strongly suggests the possibility that a low-frequency long-wavelength ($\lambda >$ length of the machine) wave exists for $B \lesssim 1.5$ kG, and this wave is causing enhanced diffusion.

A spectrum analyzer was used to examine the spectrum of both $\Delta\phi_f$ and ΔN as a function of B. These results can be seen in Fig. X-22. A definite low-frequency wave

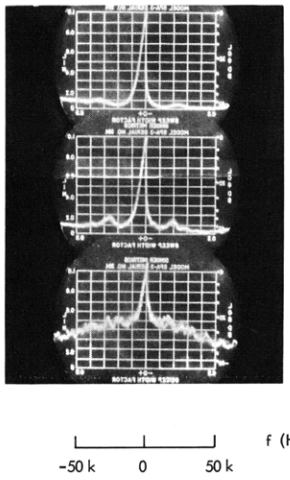

Fig. X-22. Spectrum-analyzer results.

($f \approx 12$ kHz) exists and decreases in amplitude when B is increased. The wave along with all of the low-frequency noise completely disappears for $B \geq 1.5$ kG. $T_i \approx 0.1\, T_e$;[7] therefore, based on classical theory, $\mu_\perp^i E_r > - D_\perp^i \nabla_\perp N$ (D is the diffusion coefficient). Given the last relationship and the fact that $E_r \approx 1$ V/cm, the relationship $\mu_\perp^i E_r \approx 10^3$ cm/sec ($\mu_\perp^i$ is mobility) follows. Therefore the measured radial flux for $B > 1.82$ kG agrees with the value predicted by collisional processes. Although this is not conclusive evidence, it is at least a strong indication that such a phenomenon may exist in the secondary plasma of the arc.

Additional information must be obtained before conclusive proof can be presented. Along with the low-frequency wave there also exists a high-frequency wave ($f \cong 750$ kHz). This wave does not disappear for $B > 1.5$ kV, and it is not clear whether this wave could also be affecting the radial flux.

M. Hudis, L. M. Lidsky

References

1. F. F. Chen et al., "Measurement of Low Plasma Density in a Magnetic Field," Phys. Fluids 11, 811 (1968).
2. J. Woo, "Study of a Highly Ionized Plasma Column in a Strong Magnetic Field," Ph. D. Thesis, Department of Nuclear Engineering, M. I. T., June 1966.
3. J. G. Laframbuise, "Theory of Spherical and Cylindrical Langmuir Probes in a Collisionless, Maxwellian Plasma at Rest," U. T. I. A. S. Report No. 100, Institute for Aerospace Studies, University of Toronto, Toronto, Canada, June 1966.
4. R. H. Huddlestone and S. L. Leonard (eds.), Plasma Diagnostic Techniques (Academic Press, New York, 1965), p. 120.
5. G. Suits (ed.), Collected Works of Irving Langmuir, Vol. 4, p. 379
6. F. Boeschoten and L. J. Derneten, "Measurements of Plasma Rotation in a Hollow Cathode Discharge," Plasma Phys. 10, 391 (1968).
7. M. Hudis, "Ion Temperatures, Charge Exchange, and Coulomb Collisions in an Argon Plasma Column," J. Appl. Phys. 39, 3297 (1968).

X. PLASMAS AND CONTROLLED NUCLEAR FUSION

C. Active Plasma Effects in Solids*

Academic and Research Staff

Prof. A. Bers
Prof. G. Bekefi

Graduate Students

Marie D. Beaudry
S. R. J. Brueck
E. V. George
C. S. Hartmann
D. A. Platts
R. N. Wallace

1. SURFACE WAVELENGTH MEASUREMENT OF MICROWAVE EMISSION FROM InSb

We have made preliminary measurements of the surface wavelength of the low-field microwave emission from n-type InSb. These measurements will help in distinguishing among possible mechanisms for generation of microwave emission.

The generating mechanisms that have been proposed involve acoustic waves,[1,2] helicon waves[3,4] or carrier waves.[5,6] All of these waves are slow waves, in that their phase velocity is much smaller than the velocity of light. For such slow waves, in the bulk and on the surface of the material, the fields outside the material, in free space, will decay exponentially away from the surface. The plane-wave dispersion relation shows that the decay constant, α, is the same as the propagation constant, β, of the wave along the surface. Thus, if a slow wave exists on the surface of InSb emitting microwave radiation, we can measure the wavelength, $\lambda = 2\pi/\beta$, by measuring the decay rate of the fields away from the surface. Since the wavelengths of various proposed generation mechanisms are very different both in magnitude and in their dependence upon applied fields and frequencies of observation, measurement of the wavelength should yield important information for determining the correct mechanism.

To measure the decay vs distance above the sample, a moving electric field probe was constructed. The probe was designed with a micrometer drive to move it precisely. Figure X-23 shows the tip of the probe and its relation to the sample. Care was taken in the construction to avoid coaxial or re-entrant cavity resonance. It should also be noted that the probe tip is large compared with the wavelengths that are expected so that changes in capacitive coupling caused by probe motion should be small. In use, the probe was connected to radiometers at 3 GHz and 30 MHz whose output was fed to a chart recorder.

*This work was supported by the National Science Foundation (Grant GK-2581).

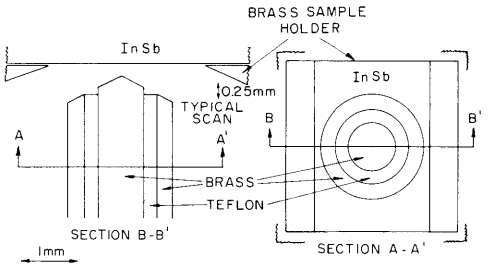

Fig. X-23. Detail views of the probe tip and its relation to the sample.

E ⊥ B

3GHz E = 40V/cm B = 8kG

B(kG)	λ (mm)	E(V/cm)	λ (mm)
6	2.5×10^{-3}	20	6×10^{-3}
8	7.7	40	7.7
10	6.2	60	10.5

30 MHz E = 40 V/cm B = 8kG

λ = 0.12 mm

E ∥ B

3GHz E=40V/cm B = 8kG B = 8kG

B E	λ (mm)	E (V/cm)	λ (mm)
+ +	5.3×10^{-3}	10	2×10^{-3}
+ −	5.5	20	2.7
− +	7.1	40	5.3
− −	5.8	60	4

30MHz E = 40V/cm B = 8kG

λ = 0.12mm

E ≮ B

3GHz E = 40V/cm B = 8kG

ANGLE, θ°	λ (mm)
0	7.7×10^{-3}
20	1.8
40	2.3
60	2.3
80	4.2
90	5.3
30 MHz 45	0.11×10^{0}

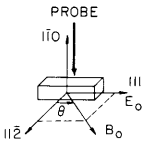

Fig. X-24. Measured wavelengths and orientations of the fields and samples.

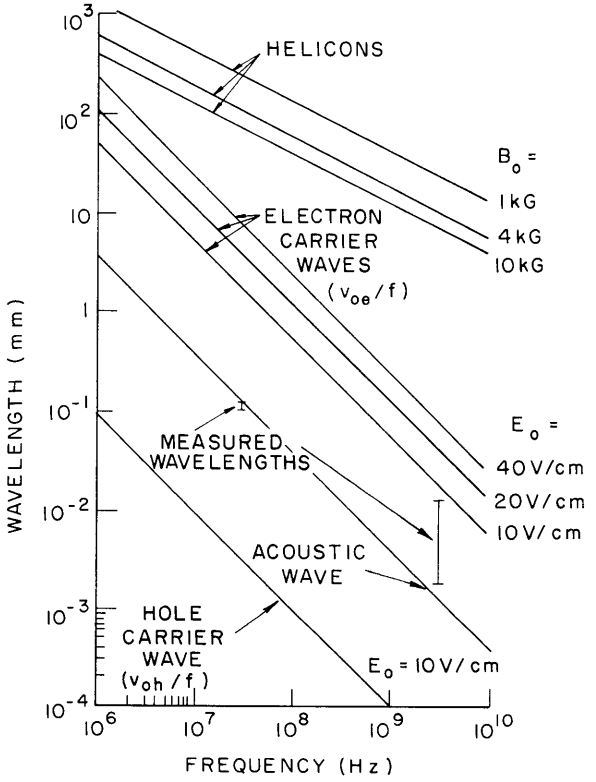

Fig. X-25. Wavelength vs frequency showing the field dependence for 3 of the possible waves. The range of the measurements is indicated.

The $2 \times 2 \times 10$ mm bar of n-type InSb was prepared by lapping the surfaces with 9.5 μ abrasive. Platinum leads were attached with indium solder. The crystal was x-ray oriented as shown in Fig. X-24. The material that was used had a mobility of 5.9×10^5 cm^2/V-sec and a density of 1.9×10^{14}/cm^3 at 77°K.

Figure X-24 gives the surface wavelengths obtained from one sample. When examining these results, one must remember that they are surface wavelengths, λ_s, which are related to bulk wavelengths, λ_β, by the angle, ϕ, of incidence of the wave on the surface:

$$\lambda_s = \frac{\lambda_\beta}{\cos \phi}.$$

Thus, the surface wavelengths can be longer than the bulk wavelengths. Figure X-25 shows the wavelengths vs frequency of some of the slow waves that have been considered as possible generating mechanisms. The experimental data are also shown. Of these waves, the acoustic wave is the best fit. Recent theoretical work (see Sec. X-C.5) has shown that in the presence of a small number of holes a two-stream instability generating waves with phase velocities close to that of the holes may also be possible. The specific variations of the wavelength with the applied fields cannot be fitted to either of these theories because the problem of preferred propagation directions in the material for given applied fields has not been worked out. More accurate measurements must be made before this is attempted.

Work is under way to improve these measurements. An interferometer is being built to measure the wavelengths by mixing the signals from a stationary probe and one that is moved along the sample. The preliminary measurements have helped in the design of such an interferometer.

D. A. Platts, A. Bers

References

1. A. Bers and T. Musha, Quarterly Progress Report No. 79, Research Laboratory of Electronics, M.I.T., October 15, 1965, pp. 104-106.
2. T. Musha and A. Bers, Bull. Am. Phys. Soc. 11, 569 (1966).
3. A. G. Chynoweth, S. J. Buchsbaum, and W. L. Feldman, J. Appl. Phys. 37, 2922 (1966).
4. G. Bekefi, Quarterly Progress Report No. 90, Research Laboratory of Electronics, M.I.T., July 15, 1968, pp. 111-118.
5. A. Bers, Quarterly Progress Report No. 73, Research Laboratory of Electronics, M.I.T., October 15, 1963, pp. 39-45.
6. P. Gueret, J. Appl. Phys. 39, 4 (1968).

2. MICROWAVE INSTABILITIES IN A SEMICONDUCTOR SUBJECTED TO DC ELECTRIC AND MAGNETIC FIELDS

We are continuing the investigation of the emission of microwave radiation from n-type InSb when a sample is subjected simultaneously to parallel DC electric and magnetic fields. It has been observed[1,2] that once certain thresholds in DC electric and magnetic fields are exceeded the emission consists of discrete spikes superposed on a background continuum. The first part of this report illustrates the frequency bandwidth, as well as magnetic-field frequency dependence of the spike emission. In previous work, the DC electric field was pulsed on for a very short time (typically 2-5 μsec) at a low repetition rate (100-200 pulses/sec) in order to prevent excessive sample heating. This made spectral analysis of the emission difficult – if not impossible. In the present work, the DC electric field was not pulsed and thus a certain amount of sample heating was tolerated. This allowed the resulting emission to be observed on a microwave spectrum analyzer.

These measurements were made on a sample (S2-7) $1.4 \times 1.4 \times 2.4$ mm, which had a mobility $\mu = 4.84 \times 10^5$ cm^2 V^{-1} sec^{-1}, and a density $n = 1.47 \times 10^{14}$ cm^{-3}, and a sample (S1-128) $1 \times 1 \times 7.6$ mm, which had a mobility $\mu = 5.9 \times 10^5$ cm^2 V^{-1} sec^{-1}, and a density $n = 2.6 \times 10^{14}$ cm^{-3}. The contacts were made by first electroplating Indium to the crystal ends and then soldering Gold wire with Indium solder to the plated surfaces. The electric field was not pulsed, but was obtained from a regulated, well-filtered DC power supply. Microwave emission, both spike and continuum, were

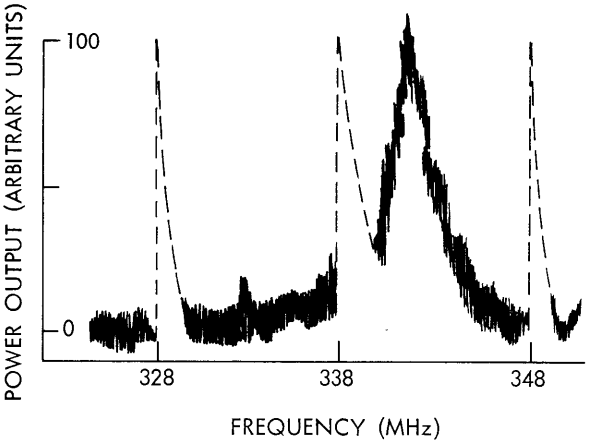

Fig. X-26.

Spectrum analyzer output. Sample S2-7. Magnetic field = 2790 G; electric field = 9 V/cm; T = 77°K.

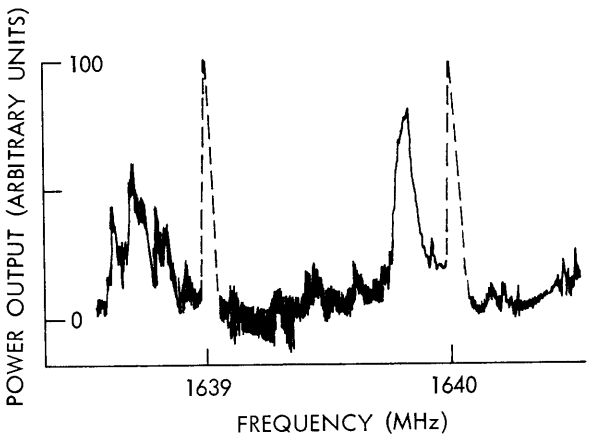

Fig. X-27.

Spectrum analyzer output. Sample S2-7. Magnetic field = 2400 G; electric field = 12 V/cm; T = 77°K.

observed from ~20 MHz up to 3 GHz. The bandwidth for the majority of reproducible spikes varied from approximately 11 MHz to approximately 4 MHz, but there did not appear to be any systematic variation of bandwidth with frequency. The output of the spectrum analyzer for a particular spike is illustrated in Fig. X-26. In varying the electric and magnetic field some very narrow-bandwidth emission was observed; this is illustrated in Fig. X-27. This type of emission was different from that of Fig. X-26, in that the very narrow-bandwidth spikes were very erratic. They appeared as bursts of noise that continually jumped in frequency, whereas the spiked emission illustrated in Fig. X-26 was steady and very reproducible from day to day.

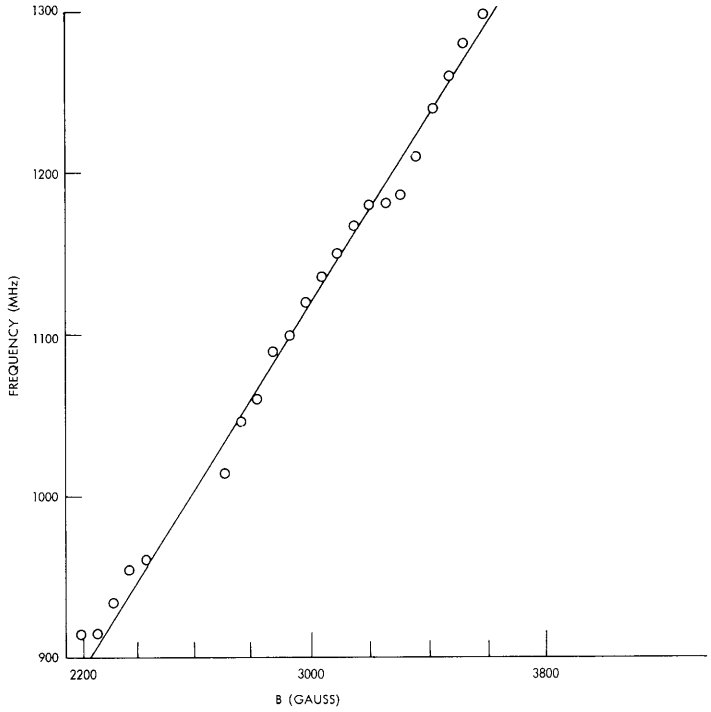

Fig. X-28. Frequency magnetic-field characteristics of a microwave spike at constant electric field (8.5 V/cm). Sample S1-128. T = 77°K.

In Fig. X-28 is illustrated the frequency of a prominent spike with varying magnetic field, at a constant electric field. It is seen that as B increases the spike moves to higher frequency. This is in contrast with the way a spike moves with electric field strength[1] at constant magnetic field; here with increasing electric field the spike moves to lower frequency.

It has been observed that identically prepared samples have different emission spectra. In most cases the samples exhibit polarity sensitive emission. We are therefore

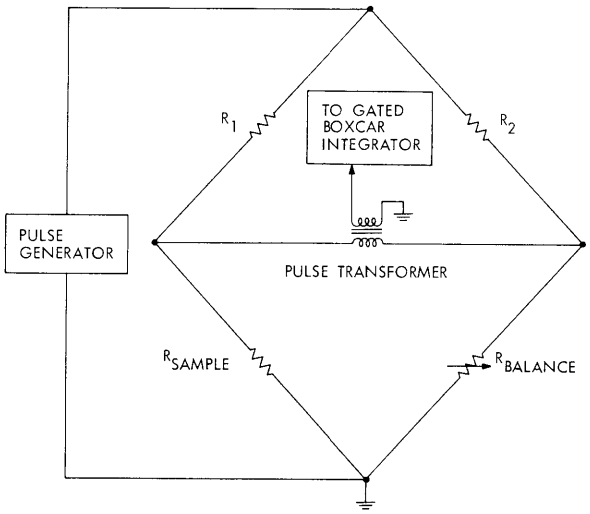

Fig. X-29.
Pulsed bridge circuit. R_1, R_2 are carbon resistors. $R_{BALANCE}$ is a high-frequency decade resistor.

considering the role (if any) played by the contacts on the emission. To facilitate this investigation, a means of very accurately measuring the resistance of the sample as the pulsed DC electric field is varied was developed. It consists of a modified Wheatstone bridge, the circuit for which is illustrated in Fig. X-29. The output of the bridge (via the boxcar integrator) is plotted on an x-y recorder as a function of the voltage across the sample. It is easy to show that the resulting plots for R_{sample} = Constant, independent of voltage, are straight lines of differing slopes, the slope being proportional to the bridge unbalance. A sample (S2-29), etched in the usual way 1.25 × 1.37 × 13.5 mm, doping and mobility being the same as for S2-7, was prepared using In-Te solder to affix the Au leads. Figure X-30 illustrates the resistance voltage characteristics for this sample as obtained from the bridge circuit. The constant-slope lines

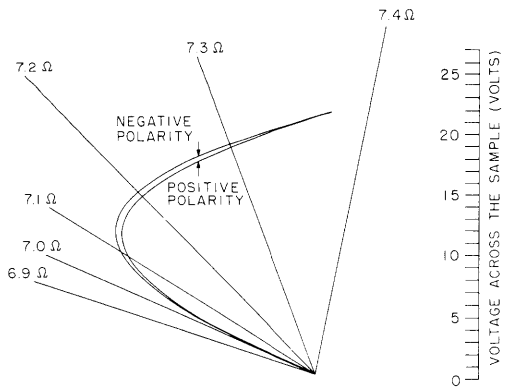

Fig. X-30.
Resistance voltage characteristics of sample S2-29 at B = 0, T = 77°K, as obtained from the bridge circuit of Fig. X-29.

(R_s = 6.9 Ω - 7.4 Ω) were obtained by substituting a high-frequency decade resistor in place of the sample. In this way, an accurate method of calibration was obtained. It is well known[3] that the mobility of charge carriers in a semiconductor is dependent on the strength of the applied electric field. This phenomenon is due to the fact that the charge-carrier distribution is no longer in thermal equilibrium with the lattice. We

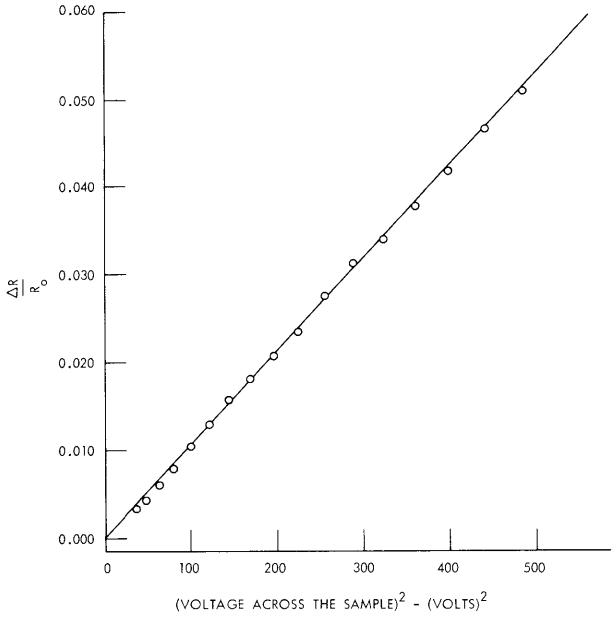

Fig. X-31. Normalized change in resistance ($\Delta R/R_o$) as a function of the square of the voltage across the sample (S2-29). R_o = 6.99 Ω, T = 77°K, B = 0.

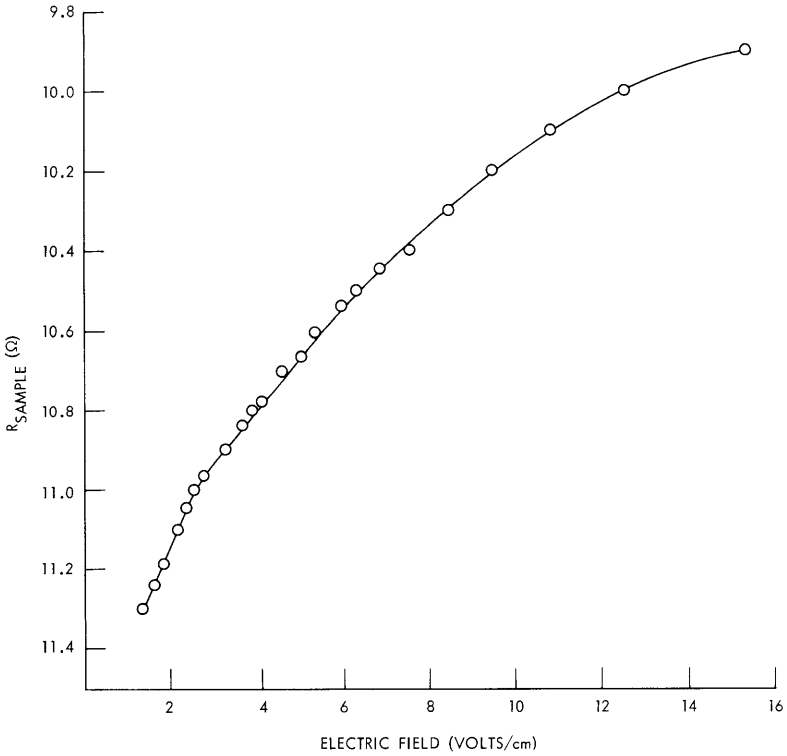

Fig. X-32. Resistance electric-field characteristics of sample S2-30C at constant magnetic field (2150 G). T = 77°K.

shall be concerned with small rises in carrier temperature, T_e, such that $(T_e-T)/T \ll 1$, where T is the lattice temperature. For such "warm" carriers the mobility is given by[4]

$$\mu = \mu_o(1+\beta E^2),$$

where μ_o is the Ohm's law mobility, E is the electric field strength, and β is a quantity that depends on the energy gain and loss rates of the carriers. Since in the low-field regime the Hall constant is constant (that is, the charge density is constant), we can write

$$\sigma = \sigma_o(1+\beta E^2),$$

or

$$R = \frac{R_o}{1 + \beta E^2},$$

where R_o is the resistance of the sample at $E \to 0$. Since βE^2 is in general small we may write

$$\frac{\Delta R}{R_o} = \frac{R - R_o}{R_o} = -\beta E^2.$$

In Fig. X-31, $\Delta R/R_o$ is plotted as a function of (sample voltage)^2 for sample S2-29. The value of β was found to be -1.8×10^{-4} cm^2 V^{-2}. No low-field microwave emission was obtained from this sample. To see if the addition of T_e played a role in determining the low-field emission, an identical sample (S2-30C), $1.4 \times 1.27 \times 10.9$ mm was prepared, using plain In to solder the Au leads to the sample. This sample showed drastic variations of resistance with electric field and no linear relation of resistance on E^2 was obtained. The resistance as a function of electric field is illustrated in Fig. X-32. This sample emitted copious amounts of microwave noise. The threshold electric field for the onset of the microwave noise at B = 2150 G was 2.75 V/cm. It appears that the contacts play an important role in the emission process, and work is now under way to determine whether the contacts provide added carriers via injection and/or provide local regions of high electric field. The latter would imply that the so-called low-field emission process is actually a form of the high-field emission process studied by Larrabee and Hicinbothem.[5]

E. V. George

References

1. E. V. George, Quarterly Progress Report No. 88, Research Laboratory of Electronics, M.I.T., January 15, 1968, pp. 202-204.
2. E. V. George, Quarterly Progress Report No. 90, Research Laboratory of Electronics, M.I.T., July 15, 1968, pp. 108-111.
3. R. J. Sladek, Phys. Rev. 120, 1589 (1960).
4. W. S. Shockley, Bell System Tech. J. 30, 990 (1951).
5. R. D. Larrabee and W. A. Hicinbothem, Jr., Proc. Symposium on Plasma Effects in Solids, Paris, France, 1964.

3. EXPERIMENTAL DETERMINATION OF CARRIER LIFETIME IN InSb

This report describes a possible method for obtaining the carrier lifetime in InSb. To create the excess carriers, a Q-switched CO_2 laser (10.6 μ), with peak powers of ~40 kW, ~200 nsec pulsewidth, was focussed onto a sample of InSb. The InSb samples were mounted in a high-speed (~1 nsec rise time) infrared detector, and the subsequent signal was capacitively coupled to an oscilloscope. Figure X-33 illustrates the detector and associated circuitry.

Samples 1 × 1 × 0.5 mm were constructed from both n- and p-type InSb. The n-type crystals had a mobility $\mu = 5.9 \times 10^5$ cm^2 V^{-1} sec^{-1} and a density $n = 2.6 \times 10^{14}$ cm^{-3}, while the p-type crystals had a mobility $\mu = 8.5 \times 10^3$ cm^2 V^{-1} sec^{-1} and a density

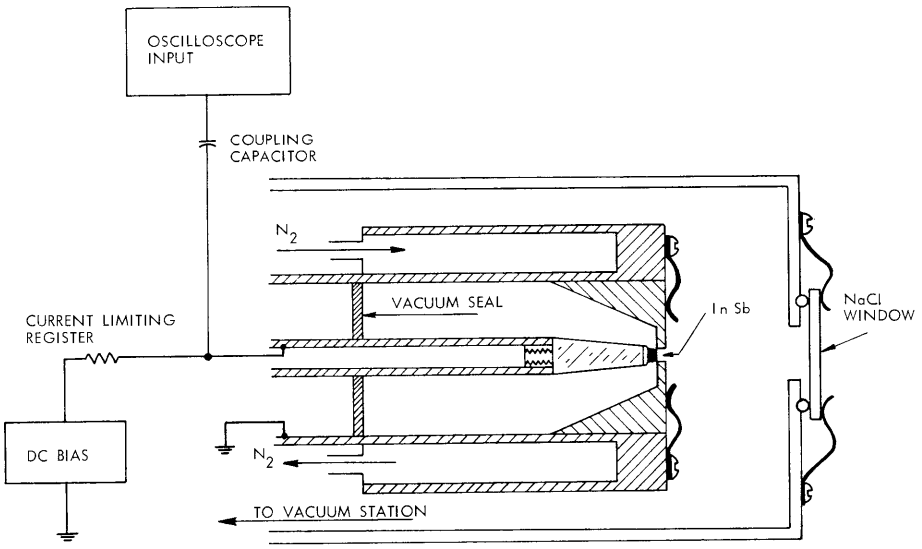

Fig. X-33. Sample holder (high-speed infrared detector) and external circuit.

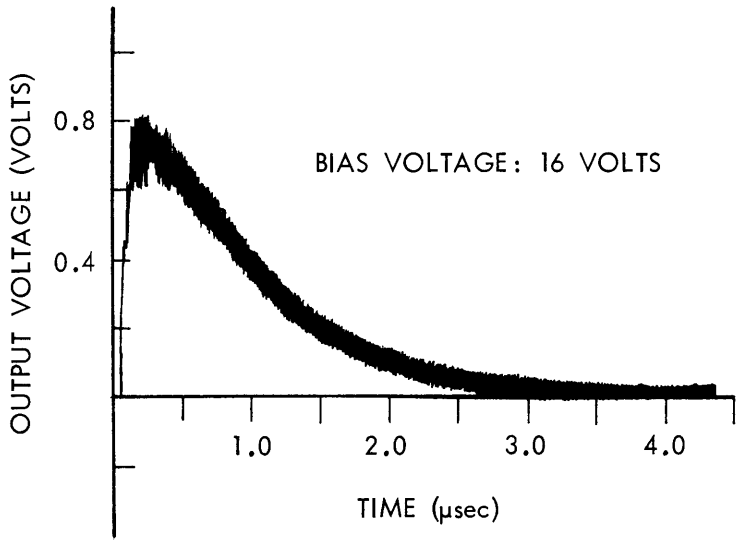

Fig. X-34. Detector output as a function of time (n-type InSb).

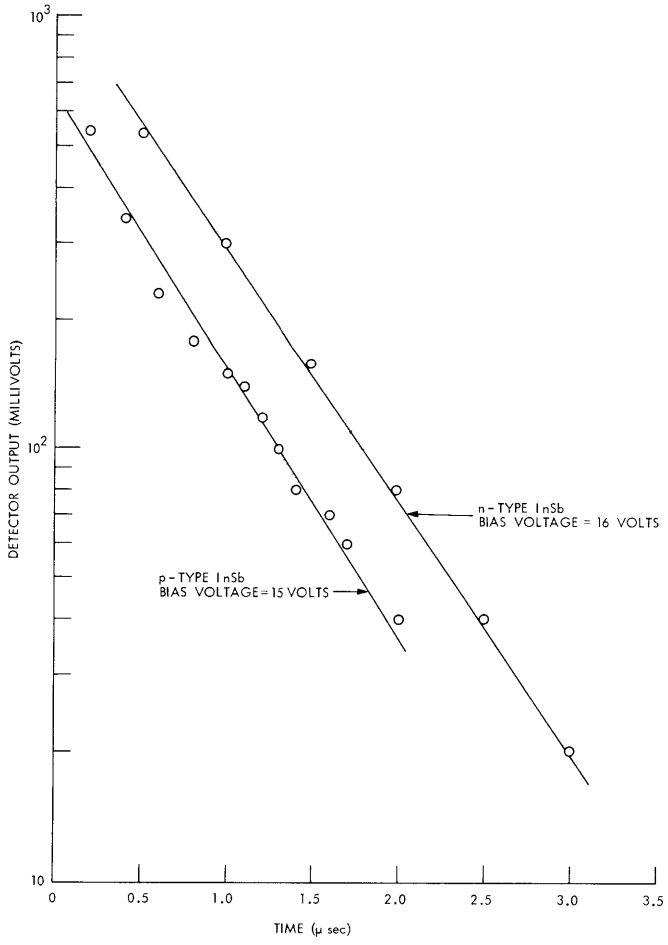

Fig. X-35.

Semi-log plot of detector output as a function of time for both n-type and p-type InSb. T = 77°K.

$n = 1.9 \times 10^{14}$ cm^{-3}. Figure X-34 illustrates the output of the oscilloscope for an n-type sample. In plotting the log (pulse height) against time a straight line was obtained, as is shown in Fig. X-35. The slope of this line yields the value of the carrier lifetime.

The values for τ were found to be $\tau_n \approx 0.77$ μsec in n-type material, and $\tau_p \approx 0.5$ μsec in p-type material. These results compare within an order of magnitude with those obtained by Laff and Fan.[1] In p-type material at 77°K, $\tau_p \gg \tau_n$. This is most likely, because of the strong trapping of electrons by donor-type centers. We had hoped that both τ_n and τ_p would be obtainable from the p-type sample, but this was not possible, perhaps on account of the poor waveform of the Q-switched laser pulse. On account of the large ratio of electron-to-hole mobility in n-type material, only the electron lifetime τ_n is determinable.

Marie D. Beaudry, E. V. George, A. S. Ratner

References

1. R. A. Laff and H. Y. Fan, Phys. Rev. 121, 53 (1961).

4. DIELECTRIC RESPONSE FUNCTION OF A PLASMA IN APPLIED ELECTRIC AND MAGNETIC FIELDS

In this report we shall give the results of a general solution to the linearized Boltzmann equation which explicitly includes both the applied DC magnetic field $\bar{B}_0$ and the applied DC electric field $\bar{E}_0$ at an arbitrary angle to $\bar{B}_0$. This allows us to determine the dielectric response function which can then be used to study various interactions, for example, acoustic wave amplification, two-stream instabilities, and so forth. Our interest here is in applying these results to plasma phenomena associated with the free carriers in a solid. The unperturbed transport properties in such plasmas are dominated by collisions. We shall, therefore, assume that a time-independent distribution function f_0 is established by the applied electric field E_0, and study perturbations that are superimposed upon this unperturbed state. As in our previous studies,[1,2] the distribution function $f(\bar{w}, \bar{r}, t)$ will be assumed to satisfy the Boltzmann equation with self-consistent fields and a collision term modeled according to Bhatnagar, Gross, and Krook.[3]

Unperturbed State

We model the free electrons in the solid by a homogeneous electron gas of density n_0, having a collision frequency ν (with the lattice) which is independent of energy, and assume an isotropic effective mass m^*. The Boltzmann equation for the unperturbed distribution function $f_0(w)$ is

$$\frac{-e}{m^*}(\bar{E}_0+\bar{w}\times\bar{B}_0)\cdot\frac{\partial f_0(w)}{\partial \bar{w}} = -\nu[f_0(w)-f_{0L}(w)], \tag{1}$$

where $f_{0L}(w)$ is the local distribution function to which the electrons relax. We shall assume that $f_{0L}(w)$ is a two-temperature Maxwellian distribution function with thermal velocities $u_{\parallel} = (\kappa T_{\parallel}/m^*)^{1/2}$ along $\bar{B}_0$ and $u_{\perp} = (\kappa T_{\perp}/m^*)^{1/2}$ across $\bar{B}_0$,

$$f_{0L}(w) = \frac{(2\pi)^{-3/2}}{u_{\parallel}u_{\perp}^2}\exp\left[-\frac{w_{\perp}^2}{2u_{\perp}^2}-\frac{w_z^2}{2u_{\parallel}^2}\right]. \tag{2}$$

We further restrict our analysis to weak electric fields E_0 such that the resultant drift velocities, $v_{0\parallel}$ along $\bar{B}_0$ and $v_{0\perp}$ across $\bar{B}_0$, are small compared with the thermal velocities ($v_{0\parallel} \ll u_{\parallel}$ and $v_{0\perp} \ll u_{\perp}$). Under these conditions, we approximate $f_0(w)$ by a drifted-Maxwellian

$$f_0(w) = \frac{(2\pi)^{-3/2}}{u_{\parallel}u_{\perp}^2}\exp\left[-\frac{(w_x-v_{0x})^2+(w_y-v_{0y})^2}{2u_{\perp}^2}-\frac{(w_z-v_{0z})^2}{2u_{\parallel}^2}\right], \tag{3}$$

where the drift velocities are determined by the applied fields $\bar{E}_0$ and $\bar{B}_0$.[4] This is summarized in Fig. X-36, with

$$v_{0\parallel} = -\mu E_{0\parallel} \tag{4}$$

$$v_{0\perp} = \frac{b}{(1+b^2)^{1/2}} \frac{E_{0\perp}}{B_0} \tag{5}$$

$$\alpha = \epsilon + \beta - \pi \tag{6}$$

$$\tan\beta = b = \mu B_0 = \frac{\omega_c}{\nu}, \tag{7}$$

where μ is the electron mobility, and ω_c is the electron-cyclotron frequency. Equations 2-5 are consistent with Eq. 1 under the stated assumption that the drift velocities remain small compared with the thermal velocities.

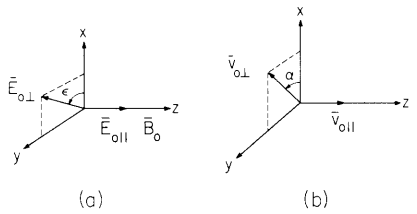

Fig. X-36. (a) Orientations of applied electric and magnetic fields.
(b) Orientations of resultant drift velocities.

Linear Response

Here we shall consider only electrostatic perturbations ($\bar{E}_1 = -\nabla\Phi_1$) for which the linearized Boltzmann equation is

$$\frac{\partial f_1}{\partial t} + \bar{w}\cdot\frac{\partial f_1}{\partial \bar{r}} + \frac{-e}{m^*}(\bar{E}_0 + \bar{w}\times\bar{B}_0)\cdot\frac{\partial f_1}{\partial \bar{w}} + \nu f_1 = \frac{en_0}{m^*}\bar{E}_1\cdot\frac{\partial f_0}{\partial \bar{w}} + \nu n_1 f_{0L}, \tag{8}$$

where $n_1 = \int f_1\, d^3w$ is the electron density perturbation that is related to the total electric field $\bar{E}_1$ through Poisson's equation. In order to solve Eq. 8 for n_1, we first transform it to a form in which the $\bar{E}_0\cdot\partial f_1/\partial\bar{w}$ term does not appear explicitly. We have previously shown[2,5] a transformation that eliminates $\bar{E}_{0\parallel}\cdot\partial f_1/\partial\bar{w}$. Moreover, to this transformation that gives $n_1 = \int g_1\, d^3w$, we now also transform coordinates in velocity space

$$\bar{w} = \bar{w}' + \bar{i}_x\frac{E_{0y}}{B_0} - \bar{i}_y\frac{E_{0x}}{B_0}, \tag{9}$$

and assuming that all perturbations vary as $\exp(-i\omega t + i\bar{q}\cdot\bar{r})$, find

$$\omega_c \frac{\partial g_1}{\partial \psi} - i(\omega' + i\nu - \bar{q}\cdot\bar{w}')\, g_1 = \frac{-ien_0}{m^*}\, \Phi_1 \bar{q}\cdot\frac{\partial g_0}{\partial \bar{w}'} + \nu n_1 g_{0L}, \tag{10}$$

where

$$\omega' = \omega - q_\perp \frac{E_{0\perp}}{B_0} \sin(\epsilon-\theta) \tag{11}$$

$$g_0(w') = \frac{(2\pi)^{3/2}}{u_{\|c} u_\perp^2} \exp\left[-\frac{(w_x'-v_{0y}/b)^2 + (w_y'+v_{0x}/b)^2}{2u_\perp^2} - \frac{(w_z'-v_{0\|})^2}{2u_{\|c}^2}\right] \tag{12}$$

$$g_{0L}(w') = \frac{(2\pi)^{3/2}}{u_{\|c} u_\perp^2} \exp\left[-\frac{(w_x'+E_{0y}/B_0)^2 + (w_y'-E_{0x}/B_0)^2}{2u_\perp^2} - \frac{w_z'^2}{2u_{\|c}^2}\right], \tag{13}$$

with

$$u_{\|c} = u_\| \left[1 + \frac{ieE_{0\|}}{q_\| \kappa T}\right]^{1/2}, \tag{14}$$

and the orientations of $\bar{q}$ and $\bar{w}'$ are as shown in Fig. X-37.

By using an appropriate integrating factor, Eq. 10 can now be solved for n_1/Φ_1.

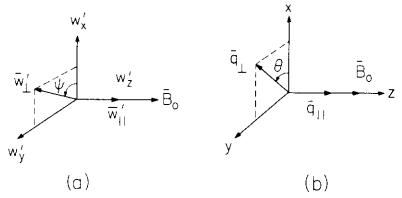

Fig. X-37. (a) Velocity-space coordinate systems oriented with respect to the applied magnetic field.
(b) Wavevectors oriented with respect to the applied magnetic field.

The longitudinal dielectric response function $K_\ell(\omega, \bar{q})$ is defined from Poisson's equation and can be written

$$K_\ell(\omega, \bar{q}) = 1 + \frac{e}{\epsilon_L q^2} \frac{n_1}{\Phi_1}, \tag{15}$$

where ϵ_L is the effective lattice dielectric constant. Hence, we find

$$K_\ell(\omega, \bar{q}) - 1 = \frac{\dfrac{\omega_p^2}{q^2 u_{\|c}^2} \sum_n e^{in(\theta-\phi)}\, e^{-\Lambda} I_n(\eta)\, \{\ \}}{1 + \dfrac{i\nu}{q_\| u_{\|c} \sqrt{2}} \sum_n e^{in(\theta-\phi_e)}\, e^{-\Lambda_e} I_n(\eta_e) Z(\zeta_n)}, \tag{16}$$

where

$$\{\ \} = \frac{Z'(\zeta_{n\|})}{2} - \frac{u_{\|c}^2}{u_\perp^2} \frac{\omega_c Z(\zeta_{n\|})}{q_\| u_{\|c} \sqrt{2}} \left[\frac{n\lambda}{\eta} \cos(\theta-\phi) + \frac{q_\perp v_b}{\omega_c} \sin(\theta-\alpha) + i\left(\eta + \lambda \frac{I_n'(\eta)}{I_n(\eta)}\right) \sin(\theta-\phi) \right] \tag{17}$$

$$\zeta_n = \frac{\omega' + i\nu - n\omega_c}{q_\| u_{\|c} \sqrt{2}} \tag{18}$$

$$\zeta_{n\|} = \frac{\omega' - q_\| v_{0\|} + i\nu - n\omega_c}{q_\| u_{\|c} \sqrt{2}} \tag{19}$$

$$\omega' = \omega - q_\perp v_e \sin(\epsilon-\theta) \tag{20}$$

$$\lambda = \left(\frac{q_\perp u_\perp}{\omega_c}\right)^2 \tag{21}$$

$$\Lambda = \lambda \left[1 + i \frac{v_b/u_\perp}{\lambda^{1/2}} \cos(\theta-\alpha) \right] \tag{22}$$

$$\eta = \Lambda \left[1 - \frac{\lambda}{\Lambda^2} \left(\frac{v_b}{u_\perp}\right)^2 \sin^2(\theta-\alpha) \right]^{1/2} \tag{23}$$

$$\tan\phi = \frac{\sin\theta + i \dfrac{v_b/u_\perp}{\lambda^{1/2}} \sin\alpha}{\cos\theta + i \dfrac{v_b/u_\perp}{\lambda^{1/2}} \cos\alpha}, \tag{24}$$

with

$$v_b = \frac{v_{0\perp}}{b} \tag{25}$$

$$v_e = \frac{E_{0\perp}}{B_0}, \tag{26}$$

and $(\Lambda_e, \eta_e, \phi_e)$ are obtained from (Λ, η, ϕ) (Eq. 22-24, respectively), by replacing v_b with v_e and the angle α with the angle ϵ. In Eq. 16 and 17, Z is the plasma dispersion function,[6] I_n is the n^{th}-order modified Bessel function, and primes on these functions denote the derivative with respect to the argument. Equation 16 is most general and rather complicated, but can be readily reduced to several special cases of interest, some of which we have treated in the past. For example, if $E_{0\perp} = 0$ but $E_{0\parallel} \neq 0$, we have $v_b = v_e = 0$, $\phi = \phi_e = \theta$, and Eq. 16 reduces to the results given in a previous report,[2] except for the fact that in the present formulation we have allowed for $u_{\parallel} \neq u_{\perp}$.

The effect of explicitly including the electric field in the Boltzmann equation can be seen by comparing Eq. 16 with the Doppler-shifted longitudinal dielectric response function which we have used in the past[1]

$$K_\ell(\omega, \bar{q}) - 1 = \frac{-\frac{\omega_p^2}{q^2 u_{\parallel}^2} \sum_n e^{-\lambda} I_n(\lambda) \left[\frac{Z'(\zeta_{nD})}{2} - \frac{u_{\parallel}^2}{u_{\perp}^2} \frac{n\omega_c Z(\zeta_{nD})}{q_{\parallel} u_{\parallel} \sqrt{2}} \right]}{1 + \frac{i\nu}{q_{\parallel} u_{\parallel} \sqrt{2}} \sum_n e^{-\lambda} I_n(\lambda)\, Z(\zeta_{nD})}, \tag{27}$$

where

$$\zeta_{nD} = \frac{\omega + i\nu - \bar{q} \cdot \bar{v}_D - n\omega_c}{q_{\parallel} u_{\parallel} \sqrt{2}}. \tag{28}$$

We note that both the real and imaginary parts of $K_\ell(\omega, \bar{q})$ from Eq. 27 can differ from those of Eq. 16. Strictly speaking, Eq. 27 is only applicable to cases in which the drift velocity is established by injection of the electrons with a drift velocity $\bar{v}_D$ and $\bar{E}_0 = 0$.

Special Cases with $E_{0\parallel} = 0$

For the special case of $\bar{E}_0 \perp \bar{B}_0$ the results are new. In this case, a simple form for $K_\ell(\omega, \bar{q})$ is obtained when $\bar{q}_\perp \parallel \bar{v}_{0\perp}$ so that $\theta = \alpha$ and therefore $\phi = \theta$. Further simplification results if we choose $\epsilon = \pi - \beta$ so that $\alpha = 0$. Then, Eq. 16 becomes

$$K_\ell(\omega, \bar{q}) - 1 = \frac{-\frac{\omega_p^2}{q^2 u_{\parallel}^2} \sum_n e^{-\Lambda} I_n(\Lambda) \left[\frac{Z'(\zeta_n)}{2} - \frac{u_{\parallel}^2}{u_{\perp}^2} \frac{\lambda}{\Lambda} \frac{n\omega_c Z(\zeta_n)}{q_{\parallel} u_{\parallel} \sqrt{2}} \right]}{1 + \frac{i\nu}{q_{\parallel} u_{\parallel} \sqrt{2}} \sum_n e^{in\phi_e} e^{-\Lambda} I_n(\eta_e)\, Z(\zeta_n)}, \tag{29}$$

where

$$\zeta_n = \frac{\omega + i\nu - q_\perp v_{0\perp} - n\omega_c}{q_{||} u_{||} \sqrt{2}} \tag{30}$$

$$\Lambda = \lambda \left[1 + i \frac{v_b/u_\perp}{\lambda^{1/2}} \right] = \lambda \left[1 + i \frac{v_{0\perp}/u_\perp}{q_\perp \ell} \right] \tag{31}$$

$$\eta_e = \lambda \left[1 - \frac{(v_e/u_\perp)^2}{\lambda} + i \frac{2v_b/u_\perp}{\lambda^{1/2}} \right]^{1/2}$$

$$= \lambda \left[1 - \left(\frac{v_{0\perp}/u_\perp}{q_\perp \ell} \right)^2 (1+b^2) + i\, 2 \frac{v_{0\perp}/u_\perp}{q_\perp \ell} \right]^{1/2} \tag{32}$$

$$\tan \phi_e = \frac{\lambda^{1/2} v_{0\perp}/u_\perp}{i\Lambda} \tag{33}$$

with $\ell = u_\perp/\nu$ the electron mean-free path. For $E_{0\perp} = 0$ and $\nu = 0$ Eq. 29 reduces to the result of Harris[7] for the anisotropic temperature plasma which may be unstable for $u_\perp^2 > 2u_{||}^2$. In the presence of an electric field, this instability condition will be modified by the factor (λ/Λ).

Finally, we consider another special case in which the propagation is entirely across $\bar{B}_0$, that is, $q_{||} = 0$. In this case, Eq. 29 reduces to

$$K_\ell(\omega, q_\perp) - 1 = \frac{-\frac{\omega_p^2}{\omega_c^2} \frac{u_{||}^2}{u_\perp^2} \sum_n \frac{e^{-\Lambda}}{\Lambda} \frac{n\omega_c I_n(\Lambda)}{\omega + i\nu - q_\perp v_{0\perp} - n\omega_c}}{1 - i\nu \sum_n e^{-\Lambda} \frac{e^{in\phi_e} I_n(\eta_e)}{\omega + i\nu - q_\perp v_{0\perp} - n\omega_c}} \tag{34}$$

where Λ, η_e, and ϕ_e are given by Eq. 31-33, respectively. For $E_{0\perp} = 0$, $u_{||} = u_\perp$, and $\nu = 0$, Eq. 34 reduces to the result of Bernstein.[8] In the presence of the electric field, the arguments of the modified Bessel functions are complex and the dielectric function is oscillatory with $q_\perp$. In fact, for $q_\perp \ell \ll (v_{0\perp}/u_\perp) \ll 1$

$$\Lambda \cong i\, \lambda \frac{v_{0\perp}/u_\perp}{q_\perp \ell} = i\lambda^{1/2} \frac{v_e}{u_\perp}, \tag{35}$$

$$\eta_e \cong i\lambda \frac{v_{0\perp}/u_\perp}{q_\perp \ell} (1+b^2)^{1/2} = i\lambda^{1/2} \frac{v_e}{u_\perp}, \tag{36}$$

and the modified Bessel functions become ordinary Bessel functions. In this case, the dielectric function may oscillate and change sign, for example, with λ (that is, the applied magnetic field). In the limit of long wavelengths ($q_\perp \to 0$) $\lambda \to 0$, and Eq. 34 may be written to first order in Λ and η_e of Eqs. 35 and 36.

$$K_\ell(\omega, \bar{q}) - 1 \cong \frac{-\omega_p^2 \omega'_\nu}{\omega_{D\perp}\left(\omega'^2_\nu - \omega_c^2\right)} \left[1 + i\lambda^{1/2} \frac{v_b}{u_\perp} \left(\frac{3\omega_c^2}{\omega'^2_\nu - 4\omega_c^2} + \frac{\omega_c^2(\omega'_\nu + i\nu)}{\omega_{D\perp}\left(\omega'^2_\nu - \omega_c^2\right)} \right)\right], \tag{37}$$

where

$$\omega'_\nu = \omega_{D\perp} + i\nu = \omega - q_\perp v_{0\perp} + i\nu. \tag{38}$$

The first term in Eq. 37, to zero order in λ, is identical with the result one would obtain from a hydrodynamic model of a cold plasma. The lowest order correction terms are proportional to $q_\perp$, in contrast to the case of no applied electric field in which the correction terms are proportional to $q_\perp^2$. Hence, in the presence of applied electric fields nonlocal effects will set in for larger wavelengths than in the absence of electric fields.

A. Bers, S. R. J. Brueck

References

1. A. Bers and T. Musha, Quarterly Progress Report No. 79, Research Laboratory of Electronics, M. I. T., October 15, 1965, p. 104.
2. A. Bers and S. R. J. Brueck, Quarterly Progress Report No. 89, Research Laboratory of Electronics, M. I. T., April 15, 1968, p. 156.
3. P. L. Bhatnagar, E. P. Gross, and M. Krook, Phys. Rev. 94, 511 (1954).
4. A. Bers, Quarterly Progress Report No. 88, Research Laboratory of Electronics, M. I. T., January 15, 1968, p. 204.
5. B. D. Fried, M. Gell-Mann, J. D. Jackson, and H. W. Wyld, J. Nucl. Energy, Part C 1, 190 (1960). This work predates the work of Pines and Schrieffer which we quoted in Quarterly Progress Report No. 89, loc. cit.
6. B. D. Fried and S. Conte, The Plasma Dispersion Function (Academic Press, Inc., New York, 1961).
7. E. G. Harris, General Atomics Report GA-5581, n. d. (unpublished).
8. I. B. Bernstein, Phys. Rev. 109, 10 (1958).

5. TWO-STREAM, ELECTROSTATIC PLASMA INSTABILITIES IN A SOLID

The instabilities of electrostatic waves associated with drifted electron-hole plasmas have received considerable theoretical attention.[1-4] Thus far, however, no clear-cut experimental verification exists for any of the proposed interaction mechanisms. Several theoretical analyses have also included an applied magnetic field,[5-7] but usually with other restrictive conditions related to specific experiments that they were trying to explain. A deficiency common to all of the theoretical analyses mentioned is that they have only considered the conditions for marginal instability (that is, the onset of temporal growth of fluctuations with real wave numbers). In this report we shall initiate a more detailed instability analysis and look for conditions for the onset of absolute instabilities. Such instabilities should be readily observed experimentally.

Absolute Instability

Consider one of the simplest situations in a solid in which the electrons are much more mobile than the holes (InSb is a favorite example). Under the action of an applied DC electric field, the electrons stream in one direction, whereas the holes move much more slowly in the opposite direction. Let us further simplify the model and assume that the electron-lattice collisions are not too frequent so that the electron-stream wave can be identified as possessing negative energy. The holes, acting as a resistive background, will drive the negative energy wave unstable. But more importantly, since the holes move in the opposite direction to the electrons, they can provide a feedback path and thus set in an absolute instability in the over-all system. For this to happen, the resistive mechanism of the holes must be either capable of moving sufficiently fast (that is, drift velocity of holes, $v_{0h} > v_{0e}$ the electron-drift velocity) or, if moving slowly, must maintain the signal that it feeds back for a sufficiently long time (that is, dielectric relaxation frequency in hole medium, $(\sigma_h/\epsilon) < \omega_{pe}$ the electron plasma frequency). The first condition is not consistent with our original assumption of holes that are much less mobile than the electrons. Hence the second condition must be satisfied sufficiently well. This leads us immediately to the conclusion that for the existence of an absolute instability it will be necessary to have much fewer holes than electrons.

A straightforward analysis of the simplest dispersion relations shows this also mathematically. First, ignoring electron-lattice collisions, we have the dispersion relation

$$1 - \frac{\omega_{pe}^2}{(\omega - qv_{0e})^2} - \frac{j(\sigma_h/\epsilon)}{(\omega + qv_h)} = 0. \tag{1}$$

It can readily be verified that the onset of the absolute instability is at $\omega = 0$ and

$q = j\omega_{pe}/v_{0e}$ and the condition for the existence of an absolute instability is

$$\frac{(\sigma_h/\epsilon)}{\omega_{pe}} \leq 2\left(\frac{v_{0h}}{v_{0e}}\right) \tag{2}$$

which can be written

$$\frac{n_h}{n_e} \leq 2\left(\frac{\nu_e}{\omega_{pe}}\right). \tag{3}$$

Since we have assumed in Eq. 1 that $\nu_e \ll \omega_{pe}$, Eq. 3 implies $n_h \ll n_e$. By including electron-lattice collisions in the dispersion relation, Eq. 1 becomes

$$1 - \frac{\omega_{pe}^2}{(\omega-qv_{0e})(\omega-qv_{0e}-j\nu_e)} - \frac{j(\sigma_h/\epsilon)}{\omega + qv_{0h}} = 0, \tag{4}$$

and the condition for the onset of an absolute instability changes from Eq. 2 to

$$\frac{(\sigma_h/\epsilon)}{\omega_{pe}} \leq \frac{v_{0h}}{v_{0e}}\left(2 - \frac{\nu_e}{\omega_{pe}}\right) \tag{5}$$

which can be written

$$\frac{n_h}{n_e} \leq \frac{\nu_e}{\omega_{pe}}\left(2 - \frac{\nu_e}{\omega_{pe}}\right). \tag{6}$$

This shows that we require $(\nu_e/\omega_{pe}) < 2$, and again a hole density smaller than the electron density.

Thermal Effects and the Action of an Applied Magnetic Field

Thermal motion of the electrons has a profound effect on the absolute instability just discussed. This is particularly true for electrons in a solid where their drift velocity v_{0e} rarely, if ever, exceeds their thermal velocity $v_{Te} = (\kappa T/m^*)^{1/2}$, and usually $v_{0e} \ll v_{Te}$. To properly account for thermal effects, a kinetic theory model should be used for describing the electron dynamics. We shall first use a simpler model based on hydrodynamic theory. The holes will still be assumed to move in a collision-dominated manner so that $\nu_h \gg (\omega+qv_{0h})$ and $\nu_h(\omega+qv_{0h}) \gg q^2v_{Th}^2$. The hydrodynamic dispersion relation is then

$$1 - \frac{\omega_{pe}^2}{(\omega-qv_{0e})(\omega-qv_{0e}-j\nu_e) - q^2v_{Te}^2} - \frac{j(\sigma_h/\epsilon)}{(\omega+qv_{0h})} = 0 \tag{7}$$

and the condition for the onset of the absolute instability at $\omega = 0$ is found to be

$$\frac{\sigma_h/\epsilon}{\omega_{pe}} \leq \frac{2\left[1 - \frac{v_{Te}^2}{v_{0e}^2}\right]^{1/2} - \frac{\nu_e}{\omega_{pe}}}{\left(1 - \frac{v_{Te}^2}{v_{0e}^2}\right)}. \tag{8}$$

From Eq. 8, we note that two conditions must be fulfilled

$$\frac{v_{Te}}{v_{0e}} < 1 \tag{9}$$

and

$$\frac{\nu_e}{\omega_{pe}} < 2\left(1 - \frac{v_{Te}^2}{v_{0e}^2}\right)^{1/2} \tag{10}$$

The condition of Eq. 9 is rather difficult to achieve in a solid. In fact, we may ask if any instability can occur at all. Solving Eq. 7 for the onset of complex frequencies at small real values of $q = q_r$, we find

$$\omega \approx -q_r v_{0h} + \delta\omega, \tag{11}$$

where

$$\delta\omega = -j\,\frac{\sigma_h}{\epsilon}\,\frac{q_r^2\left[(v_{0e}+v_{0h})^2 - v_{Te}^2\right]}{\omega_{pe}^2 - j\left(\frac{\sigma_h}{\epsilon}\right) q_r(v_{0e}+v_{0h}+v_{Te})}. \tag{12}$$

Hence, for $\mathrm{Im}(\delta\omega) < 0$ we require

$$v_{0e} + v_{0h} > v_{Te} \tag{13}$$

which is the condition for any instability to occur and is also difficult to achieve in a solid.

An applied magnetic field can be used to reduce the thermal diffusion of the electron bunching. This we have shown previously in a different context.[8] We can assume that the applied magnetic fields are moderate, so that their effect on the much more massive holes is negligible ($\omega_{ch}/\nu_h \ll 1$), but at the same time the electrons' motion is strongly

affected ($b \equiv \omega_{ce}/\nu_e \gg 1$). Under these conditions, if the magnetic field is applied across the DC electric field, the thermal velocity of the electrons, as well as the effective electron plasma density, are effectively reduced by a factor b. Equation 8 for the onset of the absolute instability may then be conjectured to require

$$\frac{\sigma_h/\epsilon}{\omega_{pe}/b} \lesssim \frac{2\left[1 - \frac{v_{Te}^2/b^2}{v_{0e}^2}\right]^{1/2} - \frac{\nu_e}{\omega_{pe}/b}}{\left(1 - \frac{v_{Te}^2/b^2}{v_{0e}^2}\right)} \tag{14}$$

which in turn requires

$$v_{0e} > \frac{v_{Te}}{b} \tag{15}$$

and

$$b\frac{\nu_e}{\omega_{pe}} \lesssim 2\left(1 - \frac{v_{Te}^2/b^2}{v_{0e}^2}\right)^{1/2} . \tag{16}$$

Conditions (15) and (16), although restrictive, are achievable in solids, and Eq. 14 can then be satisfied, provided $n_h \ll n_e$. Since large values of b may be easily achieved, somewhat easier conditions (particularly than Eq. 16) may be expected if the DC electric field is not exactly across the applied magnetic field, for then the effective electron density is reduced by a factor smaller than b. A complete analysis of this situation has just been undertaken. The dispersion relation for this case is

$$1 - \frac{\omega_{pe}^2 B^2}{(\omega - \bar{q}\cdot\bar{v}_{0e})(\omega - \bar{q}\cdot\bar{v}_{0e} - j\nu_e) - q^2 v_{Te}^2 B^2} - \frac{j\left(\frac{\sigma_h}{\epsilon}\right)}{(\omega + \bar{q}\cdot\bar{v}_{0h}) - jq^2 v_{Th}^2/\nu_h} = 0, \tag{17}$$

where

$$B^2 = \frac{1 + b^2F^2\cos^2\theta}{1 + b^2F^2} \tag{18}$$

$$F^2 = \left[1 - \frac{\omega - \bar{q}\cdot\bar{v}_{0e}}{j\nu_e}\right]^{-2} \tag{19}$$

and θ is the angle between $\bar{q}$ and $\bar{B}_o$. A computer (M.I.T. Project MAC Kludge-Display)

stability analysis of this dispersion relation has been carried out for parameters relevant to n-type InSb at 77°K. With a 10-kG magnetic field applied at 45° to the DC electric field, a fast growing absolute instability is achieved for $v_{Te} \sim 1.1\, v_{0e}$ and $n_h \approx 10^{-2} n_e$. Under these conditions, the frequency of the absolute instability is approximately $(3-j) \times 10^{-3} \omega_{pe}$ and the wave number is approximately $(-5+j) \times 10^{-1} \omega_{pe}/v_{0e}$, corresponding to a phase velocity of approximately $10^{-2} v_{0e} \approx v_{0h}$. In view of our recent measurements of the surface wavelength of microwave emission from InSb (see Sec. X-C.1), these results offer a new possible mechanism for the generation of the observed emission.

Further studies will continue for finding other suitable parameters for observing this absolute instability. In conclusion, it should be clear that a more refined dispersion relation based on kinetic theory (see Sec. X-C.4) should be used to check our simplified calculations based on Eq. 17.

A. Bers

References

1. D. Pines and J. R. Schrieffer, Phys. Rev. 124, 1387 (1961).
2. M. J. Harrison, J. Phys. Chem. Solids 23, 1079 (1962).
3. V. L. Bonch-Bruyevich and Yu. V. Gulyayev, Radiotekhnika i Elektronika 8, 1157 (1963).
4. S. Tosima and R. Hirota, J. Appl. Phys. 34, 2993 (1963).
5. A. Hasegawa, J. Appl. Phys. 36, 3590 (1965).
6. B. B. Robinson, RCA Review 28, 366 (1967).
7. P. Gueret, J. Appl. Phys. 39, 2136 (1968).
8. A. Bers, Quarterly Progress Report No. 88, Research Laboratory of Electronics, M.I.T., January 15, 1968, p. 204.